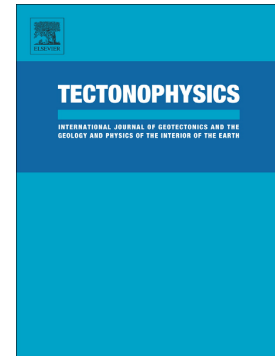


Pressure, temperature and lithological dependence of seismic and magnetic susceptibility anisotropy in amphibolites and gneisses from the central Scandinavian Caledonides

Mohsen Bazargan, Hem Bahadur Motra, Bjarne Almqvist, Sandra Piazzolo, Christoph Hieronymus



PII: S0040-1951(21)00395-4

DOI: <https://doi.org/10.1016/j.tecto.2021.229113>

Reference: TECTO 229113

To appear in: *Tectonophysics*

Received date: 20 January 2021

Revised date: 13 October 2021

Accepted date: 18 October 2021

Please cite this article as: M. Bazargan, H.B. Motra, B. Almqvist, et al., Pressure, temperature and lithological dependence of seismic and magnetic susceptibility anisotropy in amphibolites and gneisses from the central Scandinavian Caledonides, *Tectonophysics* (2021), <https://doi.org/10.1016/j.tecto.2021.229113>

This is a PDF file of an article that has undergone enhancements after acceptance, such as the addition of a cover page and metadata, and formatting for readability, but it is not yet the definitive version of record. This version will undergo additional copyediting, typesetting and review before it is published in its final form, but we are providing this version to give early visibility of the article. Please note that, during the production process, errors may be discovered which could affect the content, and all legal disclaimers that apply to the journal pertain.

Title: Pressure, temperature and lithological dependence of seismic and magnetic susceptibility anisotropy in amphibolites and gneisses from the central Scandinavian Caledonides

Mohsen Bazargan<sup>1</sup>, Hem Bahadur Motra<sup>2</sup>, Bjarne Almqvist<sup>1</sup>, Sandra Piazzolo<sup>3</sup>, Christoph Hieronymus<sup>1</sup>

<sup>1</sup>. Department of Earth Sciences, Uppsala University, Villavägen 16, 752 36, Uppsala, Sweden

<sup>2</sup>. Institute for Geosciences, Christian Albert University of Kiel, Kiel, Germany

<sup>3</sup>. School of Earth and Environment, Institute of Geophysics and Tectonics, University of Leeds, Leeds, United Kingdom

## Abstract

As a petrofabric indicator, anisotropy of magnetic susceptibility (AMS), can potentially be used to infer seismic properties of rocks, and in particular seismic anisotropy. To evaluate the link between AMS and seismic anisotropy we present laboratory measurements of elastic wave velocities and anisotropy of magnetic susceptibility (AMS) for eight samples from the deep drilling investigation forming a part of the Collisional Orogeny in the Scandinavian Caledonides (COSC) project. The samples consist of a representative suite of mid crustal, deformed rock types, namely felsic and biotite-rich gneisses, and amphibolites (mafic gneisses). Compressional (P) and shear (S) waves were measured at confining pressures from ambient to 600 MPa and temperature from room condition to 600 °C. Seismic anisotropy changes with increasing temperature and pressure, where the effect of pressure is more significant than temperature. Increasing pressure results in an increase in mean wave speed values from 4.52 to 7.86 km/s for P waves and from 2.75 to 4.09 km/s for S waves. Biotite gneiss and amphibolite exhibit the highest anisotropy with P wave velocity anisotropy (AVp) in the ranges of ~9% to ~20%, and maximum S- wave anisotropy exceeds 10 %. In contrast, Felsic gneisses are significantly less anisotropic, with AVp of <7 % and AVs of <6 %. Up to 20 % anisotropy may be generated by microcracks at 600 MPa and 600 °C, which is likely originating from thermal expansion of anisotropic minerals. An agreement is found between AMS and seismic anisotropy, although this is only a case if mean magnetic susceptibility ( $k_{\text{mean}}$ ) ranges between  $\sim 1 \times 10^{-5}$  to  $\sim 1 \times 10^{-3}$  [SI]. Such  $k_{\text{mean}}$  values are common in rocks dominated by paramagnetic matrix minerals. Based on our results we propose that such samples are the most likely to be useful for the prediction of seismic anisotropy based on their AMS data.

Keywords: Seismic anisotropy, Anisotropy of magnetic susceptibility, Petrophysics, Amphibolite, Gneiss, Scandinavian Caledonites

## 1. Introduction

Laboratory measurements of seismic anisotropy provide petrophysical signatures that allow insight into the structure of the middle and lower crust. A considerable database of seismic properties of rocks exists today for samples with known composition and structure (e.g., Birch, 1960; 1961; Christensen, 1965; 1971; 1974; 1979; Fountain, 1976; Kern, 1982; Kern et al., 1991; 1997; Burke and Fountain, 1990; Burlini and Fountain, 1993; Ji et al., 2002). Over the last two to three decades the availability of geophysical observations of the seismic structure and anisotropy in different crustal settings (e.g., Hirn et al., 1987; Shapiro et al., 2004; Schulte-Pelkum et al., 2005) has resulted in an increased interest in anisotropy sources in the middle and lower crust. Barruol and Kern (1996) experimentally inferred the effects of crystallographic preferred orientation on seismic anisotropy and shear wave birefringence for rocks that originated from the Ivrea-Verbano zone, which is a type section for the lower continental crust. Lloyd et al. (2009; 2011) and Tatham et al. (2008) argue that

observed seismic anisotropy in the middle and lower crust can be explained mainly by CPO of mica (e.g., biotite and muscovite) and amphibole, based on microstructure-based calculations. These two groups of minerals are among the most anisotropic in the crustal mineral inventory and tend to develop strong CPO's in ductile deformed rocks (Fountain et al., 1976; Burlini and Fountain, 1993; Cholach and Schmitt, 2006). Almqvist and Mainprice (2017) provide a comprehensive overview of common minerals in the continental crust and their microstructures affect seismic anisotropy.

A ductile deforming crust will result in the formation of a petrofabric, which is reflected in the expression of physical properties. It is well established that elements of petrofabric, such as crystallographic preferred orientation and shape preferred orientation, and seismic anisotropy are strongly correlated (e.g., Mainprice and Nicolas, 1989; Siegesmund et al. 1989; Mainprice, 1990; Burlini and Fountain, 1993; Barruol and Kern, 1996; Mainprice, 2000; Lloyd et al. 2005; Mainprice, 2007; Tatham and Lloyd 2008; Lloyd et al. 2009; Lloyd et al. 2011a; Lloyd et al. 2011b; Mainprice, 2015; Cyprych et al., 2017; Almqvist and Mainprice, 2017). Most of these are calculations based on quantitative constraints on crystallographic orientation data utilizing universal stage measurements, X-ray diffraction, neutron diffraction and electron backscatter diffraction (EBSD) analyses (e.g., Barruol et al., 1992; Barruol and Kern, 1996; Crosson and Lin, 1971; Valcke et al., 2006; Wenk et al., 2012). In contrast to the aforementioned methods, anisotropy of magnetic susceptibility (AMS) provides a rapid and fairly inexpensive technique (Borradaile and Henry, 1997; Borradaile and Jackson, 2010). AMS is related to the sum of the magnetic contributions from all minerals in a sample, although it is more strongly influenced by ferromagnetic minerals, such as magnetite and pyrrhotite (e.g., Hrouda, 1971; Henry, 1983; Lagroix and Borradaile, 2000). For magnetic fabric studies, the motion in the flow plane is expected to be parallel to the maximum principal axis ( $k_{\max}$ ) because the motion aligns minerals within the magnetic foliation plane ( $k_{\max}$ - $k_{\text{int}}$ ) and parallel to the flow direction. This suggests that  $k_{\max}$  is parallel to the mineral lineation and the minimum principal axis ( $k_{\min}$ ) aligns with the pole to foliation. This information provides access to specifics of magmatic fabrics in igneous rocks (e.g., Khan, 1962; Knight and Walker, 1988; Ellwood and Whitney, 1980; Bazargan et al, 2019; Vachon et al., 2021) and their tectonic settings and deformations conditions (e.g., Graham, 1966; Borradaile and Henry, 1997; Borradaile and Jackson, 2010; Mamtani et al. 2011). Furthermore, the pressure, temperature and deformation conditions may lead to new mineral growth and therefore modify the magnetic fabric (Borradaile and Jackson, 2004). The fast measurement procedure of AMS allows the evaluation of many samples, enabling a statistical approach to study the petrofabric.

Our study uses samples retrieved through the Collisional Orogeny in the Scandinavian Caledonides (COSC) continental drilling project (Lorenz et al., 2015; 2021). Reflection seismological studies were carried out at the COSC-1 site (Juhlin, et al., 2016; Hedin et al., 2012; Hedin et al., 2014; Hedin et al., 2016; Elger et al., 2021). Simon et al. (2017; 2019) presented seismic tomography and anisotropy results from surface and in the borehole to illustrate and show the anisotropy effect with case scenarios of different Thomsen parameters (Thomsen, 1986) to better explain and present the seismic wave data collected at the surface and measurements in the borehole. Additionally, several laboratory petrophysical studies investigated the seismic and magnetic properties of the COSC drill core (Wenning et al., 2016; Merz et al., 2019; Kästner et al., 2020). Merz et al. (2019) studied petrofabrics using AMS in the lower part of the borehole (1910 to 2450m) and showed the transition of magnetic mineral and periodic appearances of mylonites in mica schists and amphibole at different depth. Notably, they demonstrated that metamorphic and deformation processes related to emplaced on the Lower Seve Nappe generated new ferromagnetic minerals, including magnetite, pyrrhotite, ilmenite and hematite.

Here, we provide new data on laboratory seismic properties and AMS measurements for the samples. AMS data is compared to seismic anisotropy to evaluate under which conditions it can be used as a proxy for seismic anisotropy.

## 2. Geological setting and sample material

The COSC-1 drill site is located in central-western Sweden (Jämtland County), situated in the central Scandinavian Caledonides (Fig. 1; Lorenz et al., 2015). Tectonostratigraphically, the drilled rock unit belongs to the Lower Seve Nappe, which is part of the Middle Allochthon (Fig. 1; Gee et al., 2010; Stephens, 2020). The COSC-1 borehole is dominated by interlaying of gneisses and amphibolites, occurring on cm- to 10's m-scale, from the surface to ~2200 meters depth. The protoliths for the gneisses are sedimentary rocks formed from passive margin sediments of the Iapetus Ocean whereas the amphibolites are interpreted to originate from dyke swarms that intruded the sediments in the passive margin (Bergman et al., 2012; Gee et al., 2010; Gee, 1978). Such interlayer of felsic gneisses and amphibolites may result in excellent seismic reflections, as shown for example in the Grenville Province, Canada (Ji et al., 1997). During orogeny, the Lower Seve Nappe rocks were incorporated in the subduction channel closing the Iapetus Ocean and experienced eclogite peak metamorphic conditions (Giuntoli et al., 2018; 2020; Holmberg, 2017). During subsequent emplacement into the crust, the unit experienced metamorphic re-equilibration at amphibolite and greenschist facies conditions (Giuntoli et al., 2020).

Accordingly, the petrophysical character of these rocks is relevant to the seismic properties and anisotropy of tectonically deformed middle to lower continental crust. Even though there are outcrops of equivalent rocks available, such rocks are expected to have been modified through weathering, exhumation and erosion resulting in changes in mineralogy, open and mineral-filled fractures and micro-cracks. These latter features may significantly influence physical properties and thus the pristine drill core samples hold an advantage over outcrop derived samples.

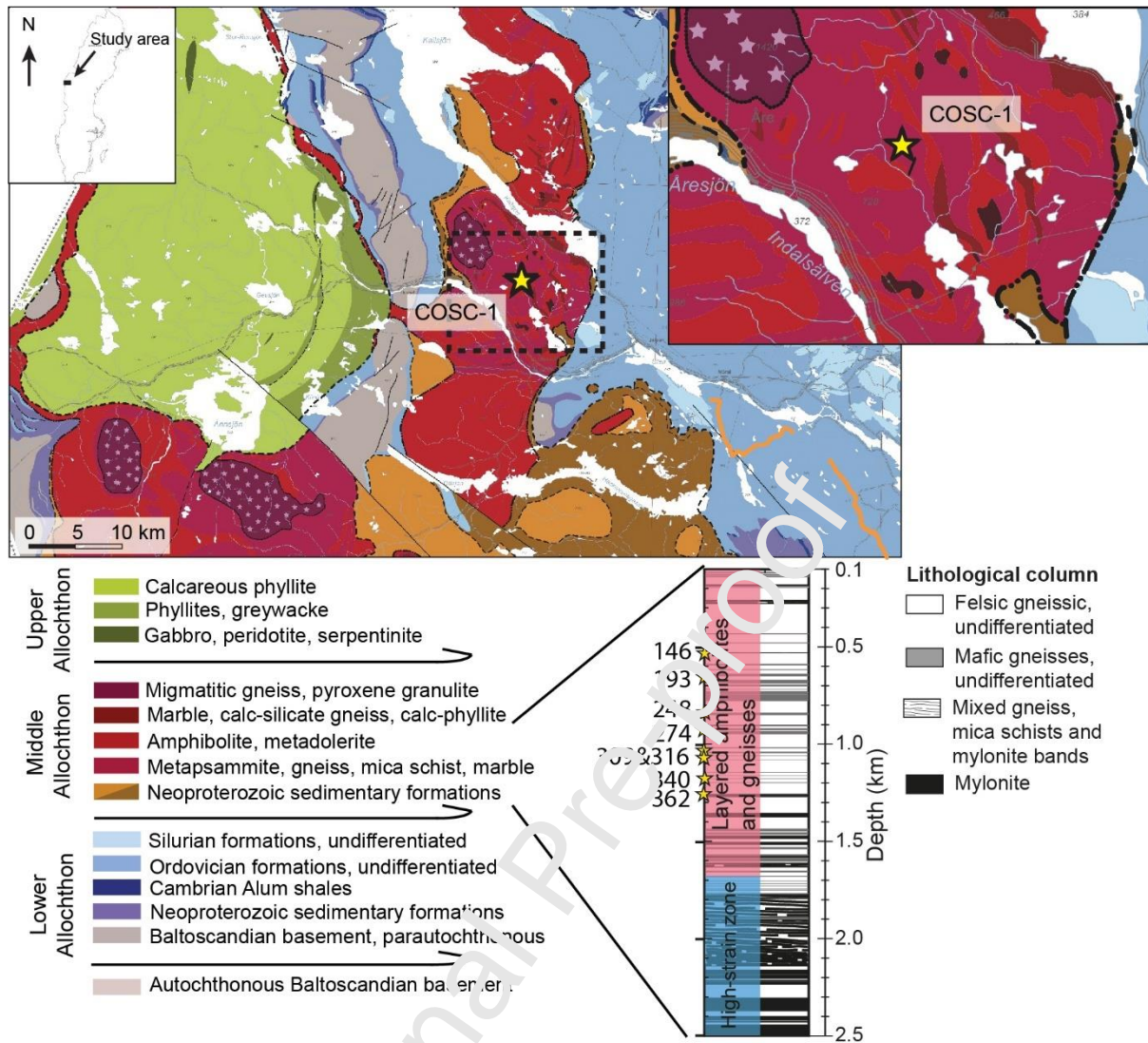


Figure 1: COSC-1 borehole location (star) shown on a regional tectonostratigraphic map of the central Scandinavian Caledonides (based on Gee et al. 1985). A simplified lithological column is provided in the lower half of the figure, which shows the locations of the samples investigated in this study and the position of the COSC-1 borehole in the generalized tectonostratigraphy of the central Scandinavian Caledonides (modified from Hedin et al., 2016).

## 2.1 Sample selection and preparation

Eight representative samples were selected from the COSC-1 drill core, originating from depths ranging from 538 m to 1243 m (Fig. 1). All samples are metamorphic and exhibit a distinct gneissic foliation characterized by alternating layers with different mineral compositions as well as mineral aggregate lineations (Piazolo & Passchier, 2002; Passchier, 2005). Samples were chosen to represent the compositional and mineralogical variation (Table 1).

From the drill core, cubic samples (43x43x43 mm) were prepared for ultrasonic measurements. Sample cubes were cut according to the fabric elements of the rocks (i.e., lineation, foliation), where the sample reference frame is defined as follows: X – parallel to the mineral lineation in the foliation plane; Y – perpendicular to the mineral lineation in the foliation plane; Z – normal to the foliation plane. In this paper, we refer to all samples based on their core related number and depth. Thin



sections were prepared from the sample cube subsequent to the ultrasonic experiment and cut perpendicular to the foliation and parallel to lineation (i.e., XZ-plane in the sample reference system).

## 2.2. Sample description

Samples are divided into rock types based on their general mineral composition, into felsic gneisses (samples 248, 309, 362), intermediate, bt-rich gneiss, i.e., biotite gneiss (sample 316) and mafic gneisses (193, 274, 340). We note that the general terms felsic, intermediate to mafic are used in a purely descriptive manner indicating dominant composition in terms of mineral abundance (e.g., felsic: dominated by quartz and feldspar). No genetic connotation is intended, i.e., magmatic or metamorphic origin. Table 1 provides a mineral modal composition for all samples.

### Felsic gneiss (FG) samples

Sample 248 (839.2 m) is dominated by medium to coarse-grained quartz and calcite, with small amounts of feldspar and muscovite, and accessory opaque phases (Table 1). Calcite is seen as large porphyroclasts (up to 1 mm) surrounded by a matrix of medium-grained (down to 100  $\mu\text{m}$ ) quartz and calcite, suggesting some degree of dynamic recrystallization. The elongation of some calcite grains defines a weak foliation barely noticeable in hand specimens but apparent in thin sections (Fig. 2a). Quartz and opaque minerals do not show significant shape preferred orientation (SPO).

Sample 309 (1021.9 m) is dominated by quartz and plagioclase feldspar; smaller amounts of K-feldspar, muscovite and opaque phases are also observed (Table 1). Quartz grains are medium to coarse-grained (a few hundred  $\mu\text{m}$  to  $>1$  mm), while plagioclase is dominantly medium-grained (a few hundred  $\mu\text{m}$ ). Grain boundaries of quartz are highly irregular and lobate and some grains exhibit undulose extinction, which suggests significant grain boundary migration, dislocation movement and subgrain formation as main deformation mechanisms. Even though individual grains show elongation, the foliation is defined by alternating bands of fine- to medium-grained plagioclase-quartz-muscovite-opaque phases and bands of  $>90\%$  coarse-grained quartz identified in hand specimen and thin section (Fig. 2b).

Sample 362 (1243.1 m) is mainly composed of plagioclase, K-feldspar and quartz, with smaller amounts of calcite, clinopyroxene and accessory opaque phases (Table 1). A clear foliation is observed in both hand specimens and thin-section. The foliation is defined by the alternation of thick bands of fine to coarse-grained feldspar with only minor clinopyroxene and bands of fine-grained mixtures of feldspar and clinopyroxene (Fig. 2c). In the thick bands, feldspar shows a clear bimodal grain size distribution, with up to 0.8 mm porphyroclasts surrounded by 100 to 300  $\mu\text{m}$  size feldspar grains. Grains show some degree of undulose extinction and elongation (SPO) of feldspar porphyroclasts is noticeable. In fine-grained bands, the clinopyroxene shows a moderate SPO with elongation subparallel to band boundaries (Fig. 3c).

### Intermediate biotite-gneiss (IBG) sample

Sample 316 (1080.0 m) is dominated by plagioclase feldspar, quartz and biotite in nearly equal parts (Table 1). A clear foliation is apparent, defined both by the preferred orientation of elongate biotite grains and planar bands dominated by biotite and bands with equal amounts of medium-grained biotite and feldspar. In these bands, biotite and feldspar show a clear SPO. However, these are less pronounced than the strong SPO seen in the biotite dominated layers (Fig. 2d); grain sizes are medium to large in biotite-dominated layers ( $\sim 100$   $\mu\text{m}$  to  $>1$  mm). Basal planes of biotite can be identified and are shown to be parallel to the foliation plane (arrows; Fig. 2d).

### Mafic gneiss (MG) samples

Sample 193 (678.2 m) is dominated by equigranular, medium-grained (50  $\mu\text{m}$  - 400  $\mu\text{m}$ ) amphibole and plagioclase with minor clinopyroxene (Table 1). Amphibole exhibit a clear SPO of tabular shaped grains whose orientation defines the foliation (3a); plagioclase also shows an SPO similar to that of amphibole. Foliation planes are evenly spaced and identifiable in the hand specimen.

Sample 274 (916.9 m) is composed of ~50 % amphibole, ~40 % plagioclase, as well as minor biotite, K-feldspar and accessory opaque phases (Table 1). Grain size ranges for amphibole from ~300  $\mu\text{m}$  to >1 mm, while the average grain size for feldspars is smaller than for amphibole. Grains are strongly interlocking and there is only a weak SPO of amphibole discernible in areas dominated by amphibole (Fig. 3b).

Sample 340 (1176.3 m) consists mainly of amphibole and feldspar and up to 15 % biotite. Grain size is largely uniform and ranges from ~500  $\mu\text{m}$  to >1 mm. Undulose extinction is seen in all three phases and all phases show a strong SPO, which defines the foliation (Fig. 3c). The SPO is most pronounced for biotite, while feldspar and amphibole show similar SPO strength. Basal planes of biotite can be identified and are shown to be parallel to the foliation plane. Foliation planes are clearly defined and tightly spaced.

#### **Layered felsic-mafic gneiss (LG)**

Sample 146 (538.6 m) is strongly banded, where banding is defined by granoblastic layers of feldspar, quartz and minor opaques (felsic layer) and layers of plagioclase-clinopyroxene gneiss (mafic layer). These layers are planar and well defined in hand specimen, ranging from 0.5 to 3 cm in thickness. The quartz-feldspar-rich layers are generally coarse-grained, although in some cases fine-grained grains surround coarser grains. The mafic layer is generally finer-grained than the quartz-feldspar layer, with a clear bimodal grain size distribution of the plagioclase and clinopyroxene. Besides the layering, there is little evidence for SPO among most of the phases (Fig. 4d) except for elongate grains of interstitial opaque phases present in both types of layers. Nevertheless, in the mafic band, the cm-scale banding is mirrored by the elongation of clusters of feldspar and/ or clusters of clinopyroxene.

Table 1. Modal mineral composition (%) of samples in the study

Sample no.	Rock type	Qz	Pl	Kfs	Cal	Amph (hbl)	Cpx (Di)	Bi	Ms	Ot <sup>a</sup> or Cr <sup>a</sup> , Ap, opq
146	Felsic gneiss	60	25	10	3-5		≤2			
193	Amphibolite	5	20			75				
248	Calc-silicate	50	≤5	≤5	35		≤5		≤5	accessory
274	Amphibole-gneiss		40	5		50		3-5		≤2
309	Felsic gneiss	50	35	15				accessory		
316	Intermediate Bt-gneiss	30	25				15	25		≤5
340	Amphibolite		30			55-60		10-15		
362	Felsic gneiss / calc-silicate	25		50-60	10-15		10			accessory

Mineral abbreviations from Whitney and Evans (2010): Qz - quartz; Pl - plagioclase; Kfs - potassium feldspar; hbl - hornblende;

Di - diopside; Bi - biotite; Mu - muscovite; Ep - epidote; Ap - apatite; opq - opaque



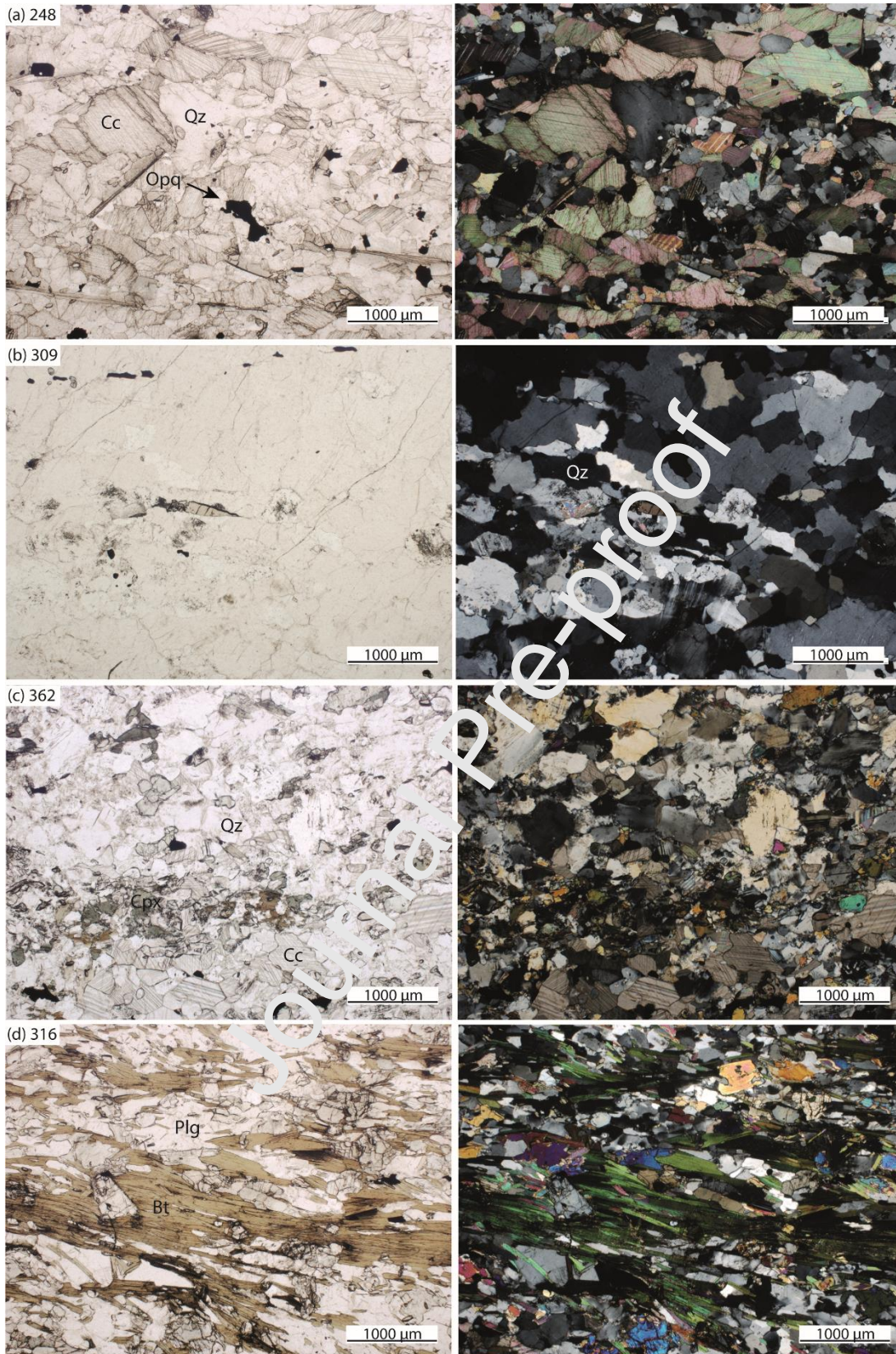


Figure 2: Photomicrographs of the (a-c) felsic gneisses (samples 248, 309, 362) and the (d) intermediate biotite-gneiss (sample 316), taken in plane-polarized (left side) and cross-polarized (right side) light. Mineral abbreviations follow Whitney and Evans (2010); Amp: amphibole; Plg: plagioclase feldspar; Cpx: clinopyroxene; Qz: quartz; Opq: opaque (generally iron-oxide or iron-sulphide).



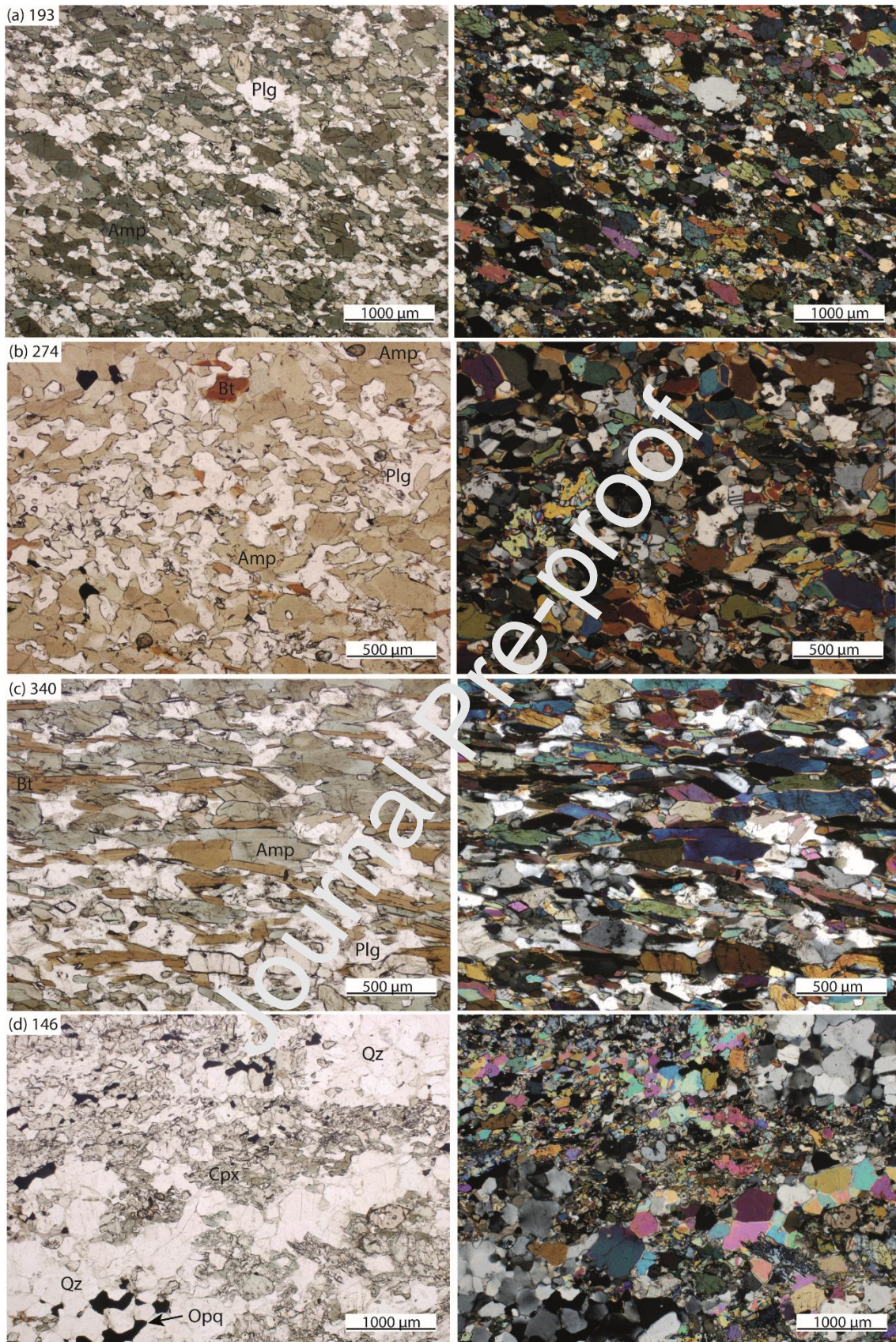


Figure 3: Photomicrographs of (a-c) mafic gneisses (samples 193, 274, 340) and (d) layered felsic-mafic gneiss (sample 146), taken in plane-polarized (left side) and cross-polarized (right side) light. Mineral identification follow Whitney and Evans (2010); Amp: amphibole; Bt: biotite; Plg: plagioclase feldspar; Qz: quartz.



### 3. Methodology

#### 3.1 Ultrasonic velocity measurements

Experiments were performed with a multi-anvil apparatus at the Institute for Geosciences at Kiel University (Germany), allowing for measurements of compressional ( $V_p$ ) and orthogonally polarised shear wave velocities ( $V_{s1}$ ,  $V_{s2}$ ). Ultrasonic velocities (P- and S-wave) were experimentally measured using the ultrasonic pulse transmission technique (Birch, 1960; Kern et al., 1990). The shear-wave transducers were oriented such that the predominant  $S_1$  and  $S_2$  particle motions were either parallel or perpendicular to foliation and lineation (Kern et al., 1997; Motra et al., 2018). Transducers were operated at 2 MHz and 1 MHz for P-wave and S-waves, respectively. The cumulative errors in both  $V_p$  and  $V_s$  were estimated to be <1% of the measured wave speed. Length and volume changes of the sample cube, resulting from changes in principal stresses, are obtained by the resulting piston displacement, which was used to correct the time-of-flight of the ultrasonic wave. Measurements were first performed at room temperature and increasing pressure up to 600 MPa, in step-wise increasing pressure increments. After the measurements during loading, the confining pressure was reduced and measurements were made during unloading (de-pressurization). Temperature-dependent measurements were made at maximum confining pressure (600 MPa), by increasing temperature from room conditions at 100 °C steps up to 600 °C. After each pressure increment, a five-minute stabilization period was used before reaching the result and 30 minutes for each temperature increment - until stable conditions are reached. The rationale behind the choice for pressure and temperature stems from the conditions expected in the crust from a setting of exhumed crust (low P and low T), buried orogenic crust (e.g., the Himalayas and the Tibetan Plateau) so that the data can be compared to acquired seismic data from both ancient, exhumed and modern orogens. In addition, initially pressurizing the sample to 600 MPa followed by increasing the temperature to 600 °C, reduces the amount of thermally induced cracking of the sample during elastic wave speed measurements. Each set of results for a sample is comprised of nine velocities, measured along the three perpendicular axes (X, Y, Z): three P-wave velocities and six S-wave velocities. Each S-wave has two polarizations,  $s_1$  and  $s_2$ , where  $s_1 > s_2$ . The ultrasonic measurements were complemented by density measurements, which were measured by dividing the measured sample volume by its mass.

Based on the measurements, we calculate the difference in shear wave speed ( $dV_s$ ), the anisotropy of the P- (%  $AV_p$ ) and S- wave (%  $AV_s$ ), and the mean  $V_p$  and  $V_s$ ,

$$dV_s = V_{s1} - V_{s2} \quad \text{Eq. 1;}$$

$$\%AV_p = \frac{V_{pmax} - V_{pmin}}{V_{pmean}} * 100 \quad \text{Eq. 2a;}$$

$$\%AV_s = \frac{V_{smax} - V_{smin}}{V_{smean}} * 100 \quad \text{Eq. 2b;}$$

$$V_{pmean} = \frac{V_{pmax} + V_{pint} + V_{pmin}}{3} \quad \text{Eq. 3a;}$$

$$V_{smean} = \frac{V_{smax} + V_{sint} + V_{smin}}{3} \quad \text{Eq. 3b.}$$

The fastest  $V_p$  and  $V_s$  directions represent  $V_{pmax}$  and  $V_{smax}$ , whereas the slowest axes are  $V_{pmin}$  and  $V_{smin}$ . Additionally, the Thomsen parameters  $\epsilon$  and  $\gamma$  Thomsen, (1986), were calculated

$$\epsilon = \frac{C_{11} - C_{33}}{2C_{33}} \quad \text{Eq. 4;}$$

$$\gamma = \frac{C_{66}-C_{44}}{2C_{44}} \quad \text{Eq. 5.}$$

$C_{11}$ ,  $C_{33}$ ,  $C_{44}$  and  $C_{66}$  are elastic constants that depend on the orientation of the sample. We assume that each sample has a transverse isotropic or orthorhombic symmetry. Elastic constants were then calculated using ultrasonic wave speed along the X, Y and Z axes, and density. It was not possible to calculate the Thomsen  $\delta$  parameter, which requires measurements at  $45^\circ$  to the symmetry axis in the sample to obtain the  $C_{13}$  elastic constant.

### 3.2 Anisotropy of magnetic susceptibility (AMS)

AMS measurements were performed on rock cubes that were cut from the blocks initially used for ultrasonic wave speed measurements. Each block was cut into eight smaller cubes with  $\sim 20$  mm sides. Measurements were made using the MFK1-FA susceptibility bridge (AGICO, Czech Republic) at the Department of Earth Sciences at Uppsala University. The measurements give the orientation and magnitude of three principal axes of the AMS ellipsoid ( $k_{\max} \geq k_{\text{int}} \geq k_{\min}$ ), which are calculated from the second-rank symmetric magnetic susceptibility tensor. All measurements were made in the semi-automatic spinning mode, with an applied alternating field of 200 A/m and a frequency of 976 Hz. The averaged values of  $k_{\max}$ ,  $k_{\text{int}}$  and  $k_{\min}$ , based on up to eight separate cubes, were used to calculate the following AMS parameters.

$$\mu 1 = \ln(K_{\max}), \mu 2 = \ln(K_{\text{Int}}), \mu 3 = \ln(K_{\min}), \mu m = \ln(K_{\text{mean}}) \quad \text{Eq. 6a;}$$

$$K_{\text{mean}} = \frac{K_{\max} + K_{\text{Int}} + K_{\min}}{3} \quad \text{Eq. 6b;}$$

$$P_j = \exp \sqrt{(2(\mu 1 - \mu m)^2 + (\mu 2 - \mu m)^2 + (\mu 3 - \mu m)^2)} \quad \text{Eq. 7;}$$

$$T_j = \frac{2\mu 2 - \mu 1 - \mu 3}{\mu 1 - \mu 3} \quad \text{Eq. 8;}$$

$$F = \frac{K_{\text{Int}}}{K_{\min}} \quad \text{Eq. 9;}$$

$$L = \frac{K_{\max}}{K_{\text{Int}}} \quad \text{Eq. 10.}$$

The degree of anisotropy,  $P_j$  (eq. 7), is indicative of the magnitude of anisotropy, which reflects generally the shape preferred orientation (SPO), and crystallographic preferred orientation (CPO) (Borradaile and Jackson, 2004). Hence, a high  $P_j$  implies the presence of stronger fabric (defined by both SPO and CPO) intensity. Even though  $P_j$  does not directly measure the strain magnitude, it may indirectly be a useful indicator for principal axes of strain and the intensity of deformation (e.g., Borradaile and Henry, 1997). The shape of the anisotropy (eq. 8) is indicated by  $T_j$  and ranges from -1 to 1, which indicates prolate or oblate shape, respectively. A value of  $T_j = 0$  represents a neutral triaxial ellipsoid with the difference of  $k_{\max}$  and  $k_{\text{int}}$  being proportional to the difference between  $k_{\text{int}}$  and  $k_{\min}$ .  $F$  and  $L$  represent the magnetic foliation and lineation in the sample.

For a better understanding of the source minerals that contribute to AMS, magnetic susceptibility was measured as a function of temperature. This test is used to identify the magnetic minerals present in the rock. The tests constitute continuous susceptibility measurements with increasing temperature, from room conditions up to 700 °C, followed by a decrease in temperature back to room conditions. For this measurement, sample material was crushed to fine-grained pieces with a milling machine and further crushed to a powder with an agate pestle and mortar. Measurements

were done with the MFK1-FA, equipped with CS-4 furnace add-on, in an inert argon gas atmosphere. The results for these measurements are presented in the online supplementary material (S1 and Fig. S1).

## 4. Results

### 4.1 Ultrasonic wave velocities (Vp and Vs)

Representative P- and S- waves velocities as a function of pressure and temperature are shown in Figures 5 to 8. Equivalent seismic wave speed figures for all samples are provided in the online supplementary material S2 (Figs. S2-S5). Tables 2 and 3 summarize the seismic properties of all samples.

#### 4.1.1. Compressional wave (Vp)

##### Felsic gneiss samples

All felsic gneiss samples show similar ultrasonic wave speeds and  $AV_p$ , where the latter ranges from 4-6 % at the highest applied pressure (600 MPa) and temperature (600 °C) (Tables 2 and 3). Sample 248 show an increase in  $V_{p,mean}$  as a function of pressure, from 4.71 to 6.41 km/s, from room conditions up to 600 MPa. The minimum and maximum P-wave velocities are 6.22 and 6.59 km/s along the Z- and X-axis, respectively. From these differences in velocity, the P-wave anisotropy at 600 MPa is 5.4%. Increasing temperature from room conditions to 600 °C (at a fixed pressure of 600 MPa), shows a drop in  $V_{p,mean}$  from 6.38 to 6.02 km/s. The minimum and maximum Vp are 5.91 and 6.26 km/s, resulting in an  $AV_p$  of 5.8%. For sample 309, mean Vp increases from 4.93 to 6.18 km/s as a function of pressurization. At 600 MPa confining pressure, the minimum and maximum Vp are along the Z and X-axes, 6.00 and 6.32 km/s, respectively, with  $AV_p$  of 5.3%.  $V_{p,mean}$  decreases slightly when increasing temperature to 600 °C, from 6.18 to 5.97 km/s. Minimum and maximum velocities are 5.80 and 6.08 km/s, along the Z- and X-axis, corresponding to an  $AV_p$  of 4.7%. In Sample 362,  $V_{p,mean}$  increases from 4.53 to 6.43 km/s from room conditions to 600 MPa (Fig. 4a). The minimum and maximum Vp at 600 MPa pressure are 6.27 and 6.64 km/s along the Z- and X- axes, respectively. From these differences, the  $AV_p$  is 5.6%. A slight decrease in Vp along with X, Y and Z-axes is observed as a function of temperature, and  $AV_p$  is ~6 % at 600 °C.

##### Intermediate, biotite-gneiss

The biotite-rich sample (316) shows generally comparably Vp to the mafic gneisses (below);  $AV_p$  is the highest observed for any sample.  $V_{p,mean}$  increases from 4.82 to 6.45 km/s, from room pressure to 600 MPa. P-wave velocities at 600 MPa along the Z- and X- axes are 5.74 and 7.01 km/s resulting in an  $AV_p$  of 19.7% (Fig. 4b).  $V_{p,mean}$  drops from 6.44 to 6.32 km/s when increasing temperature to 600 °C (Fig. 5b), and  $AV_p$  increases to 23.8% (from the minimum and maximum Vp of 5.50 and 7.01 km/s).

##### Mafic gneiss samples

For sample 193, mean Vp increases from 5.23 to 7.07 km/s, from room pressure to 600 MPa (Fig. 4c). At 600 MPa pressure, the minimum and maximum Vp are 6.61 and 7.49 km/s along the Z- and X- axes, respectively;  $AV_p$  at 600 MPa is 12.2%. P-wave velocity shows a slight drop due to increasing

temperature to 600 °C for  $V_{p_{mean}}$ , from 7.11 to 6.91 km/s. At 600 °C, the minimum and maximum velocities are 6.42 and 7.36 km/s; correspondingly AVp increased to 13.6% (Fig. 5c). For sample 274  $V_{p_{mean}}$  increases from 5.52 to 6.89 km/s, during pressurization from room conditions to 600 MPa. The minimum and maximum P-wave velocities at 600 MPa pressure are 6.65 and 7.33 km/s along the Y- and X-axis, resulting in 9.7% AVp (note that Vp along with Y- and Z-axes are similar for this sample).  $V_{p_{mean}}$  shows a drop from 6.9 km/s to 6.89 km/s when increasing temperature to 600 °C. The minimum and maximum velocities at 600 °C are 6.52 and 7.21 km/s, along the same axes as during pressurization, resulting in 10.0% AVp. In sample 340  $V_{p_{mean}}$  increases from 4.70 to 7.05 km/s. At 600 MPa pressure the minimum and maximum Vp are 6.33 and 7.60 km/s along the Z- and X- axes, respectively, resulting in an AVp of 17.9%. The increasing temperature to 600 °C leads to a drop in  $V_{p_{mean}}$  from 7.08 to 6.91 km/s. Minimum and maximum velocities are 6.12 and 7.54 km/s, resulting in an AVp of 18.0 %.

### Layered felsic-mafic gneiss

Sample 146 results show that  $V_{p_{mean}}$  changes from 5.23 to 6.93 km/s, as a function of pressure (Fig. 4d). At 600 MPa pressure, the minimum and maximum P-wave velocities are 5.94 and 6.49 km/s. P wave anisotropy at 600 MPa is 8.9%. P-wave velocity shows a slight drop due to the temperature increase, from 6.26 to 6.04 km/s. At 600 °C the minimum and maximum velocities were 5.73 and 6.33 km/s, along the X-axis and Z-axis, respectively (Fig. 6d); AVp at 600 MPa and 600 °C increased to 10.1%.



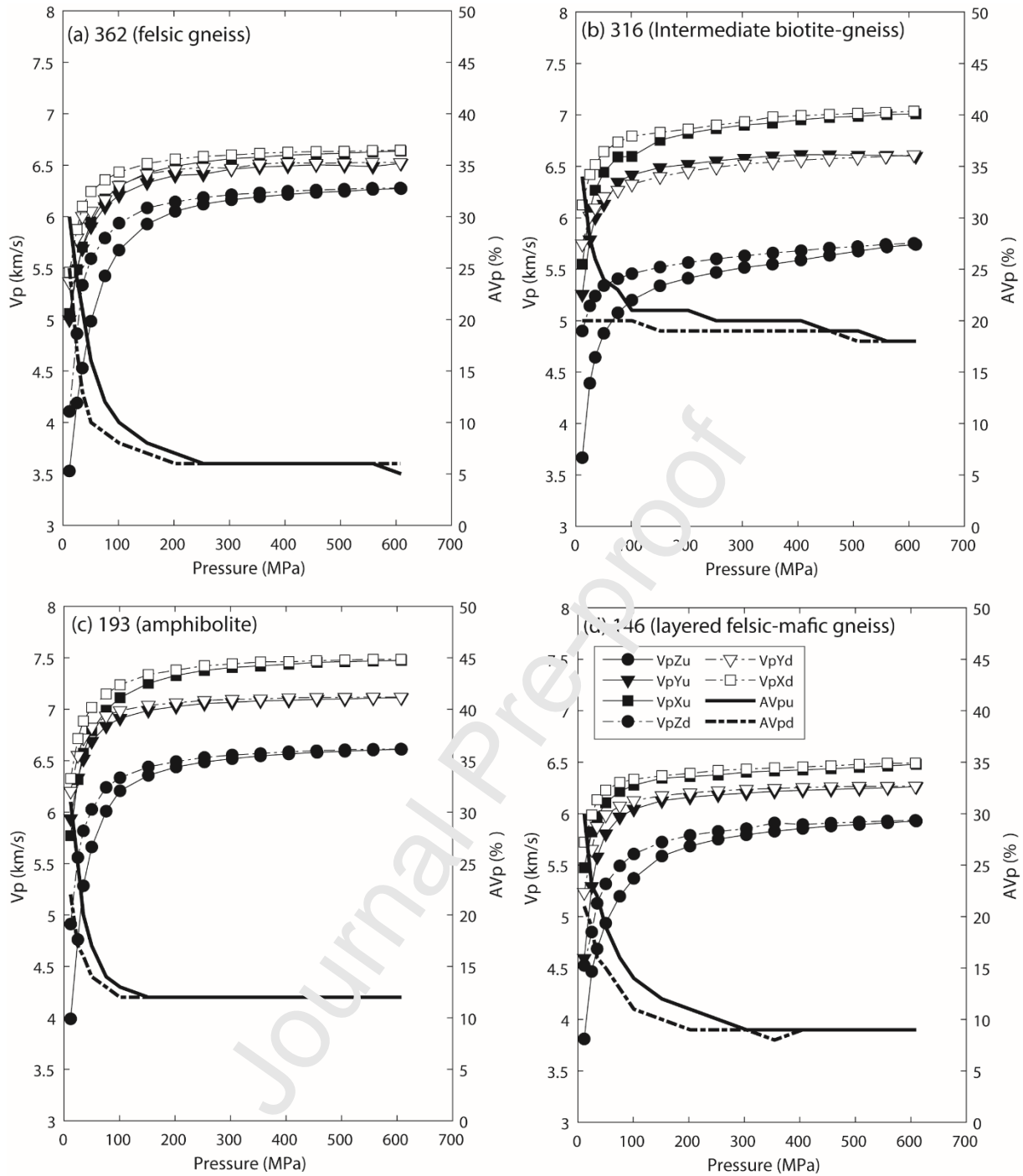


Figure 4: P-wave velocity ( $V_p$ ; left y-axis) and anisotropy of  $V_p$  (AVp, right y-axis) as a function of confining pressure for four selected samples investigated in this study, (a) felsic gneiss (362), (b) intermediate biotite-gneiss (316), (c) amphibolite (mafic gneiss; 193) and (d) layered felsic-mafic gneiss (146). The filled circles show  $V_p$  during pressurization and the open circles represent  $V_p$  during depressurization. Letters u and d in the legend indicate measurements performed during pressurization and de-pressurization, respectively.

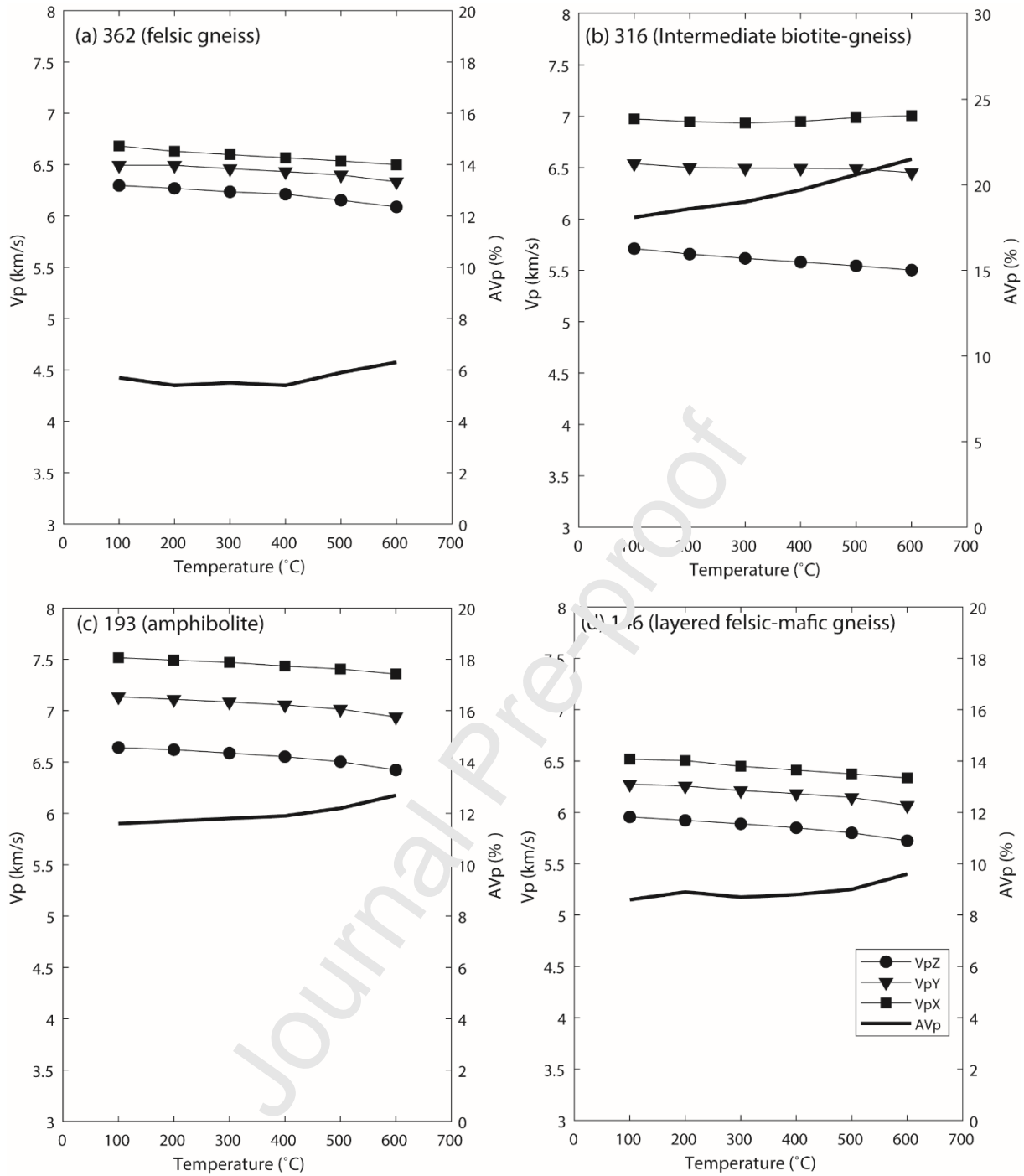


Figure 5: P wave velocity ( $V_p$ ; left y-axis) and anisotropy of  $V_p$  (AVp, right y-axis) as a function of temperature for samples (a) 362 – felsic gneiss; (b) 316 – Intermediate biotite-gneiss; (c) 193 – amphibolite; (d) 146 – layered felsic-mafic gneiss. All measurements were made at a fixed pressure of 600 MPa.

#### 4.1.2. Shear wave velocities ( $V_{s1}$ , $V_{s2}$ ) and shear wave splitting (dVs)

##### Felsic gneiss samples

As with P-wave velocities, shear wave speeds increase as a function of pressure and decrease slightly as a function of increasing temperature. Shear wave splitting is generally highest along X- and Y-axes,

whereas minimum splitting occurs along the Z-axis. Results are shown in Figures 6 and 7 and in Tables 2 and 3.

### **Felsic gneiss samples**

At 600 MPa, sample 248 exhibits dVs along X, Y and Z axes of 0.008, 0.099 and 0.119 km/s, and at 600 MPa and 600°C, the dVs has increased slightly, to 0.01, 0.11 and 0.14 km/s. Sample 309 exhibits fairly low dVs and at room temperature and maximum confining pressure, the dVs along the X, Y and Z axes are 0.153, 0.003 and 0.151 km/s, respectively, and at 600 MPa and 600 °C, the respective axes show dVs of 0.033, 0.003 and 0.109 km/s. Shear wave splitting for sample 362 (Felsic gneiss) is minimum along the X-axis; splitting along the Y-axis is highest and along the Z-axis it is intermediate (Fig. 7a). This is similar for room temperature conditions and 600 MPa confining pressure, and applying temperature to 600 °C (Fig. 8a). The dVs under pressure condition are 0.01, 0.14 and 0.151 km/s and in fixed 600MPa pressure and 600 °C are 0.005, 0.141 and 0.122 Km/s along X-, Y- and Z-axes, respectively.

### **Intermediate, biotite-gneiss**

Sample 316 exhibits maximum splitting along the X- and Y-axes. This trend remains similar from room temperature and increasing pressure with dVs of 0.475, 0.578 (Fig. 7b) and 0.036 km/s to fixed 600 MPa pressure and 600 °C (Fig. 8b) with dVs of 0.01, 0.809 and 0.133 km/s along X, Y and Z-axes.

### **Mafic gneiss samples**

For sample 274, dVs remains similar at maximum confining laboratory conditions pressure (600 MPa), compared to maximum pressure and temperature (600 °C). The dVs under these conditions along X, Y and Z axes are 0.01, 0.22, 0.19 km/s and 0.02, 0.10, 0.24 km/s, respectively. Sample 193 shows maximum shear wave splitting along the X-axis and minimum splitting along the Z-axis. The differences between  $V_{s1}$  and  $V_{s2}$  at room temperature and 600 MPa are, along X, Y and Z axes, 0.06, 0.31 and 0.33 km/s, respectively (Fig. 7c). At 600MPa and 600°C, are 0.048, 0.288 and 0.343 km/s (Fig. 8c). Sample 340, shows maximum splitting along Y and X-axes and minimum splitting along the Z-axis. Its dVs 600 MPa and room temperature, along the X-, Y- and Z-axes, are 0.008, 0.633 and 0.737 km/s and at 600MPa pressure and 600°C temperature in X, Y and Z axis are 0.004, 0.637 and 0.722 km/s.

### **Layered felsic-mafic gneiss sample**

Sample 146 shows relatively small shear wave splitting overall, with maximum splitting along the Y-axis, whereas the smallest splitting occurs along the X- and Z-axes. This trend remains similar at 600 MPa (Fig. 7d) and 600 °C (Fig. 8d), although it is somewhat reduced.

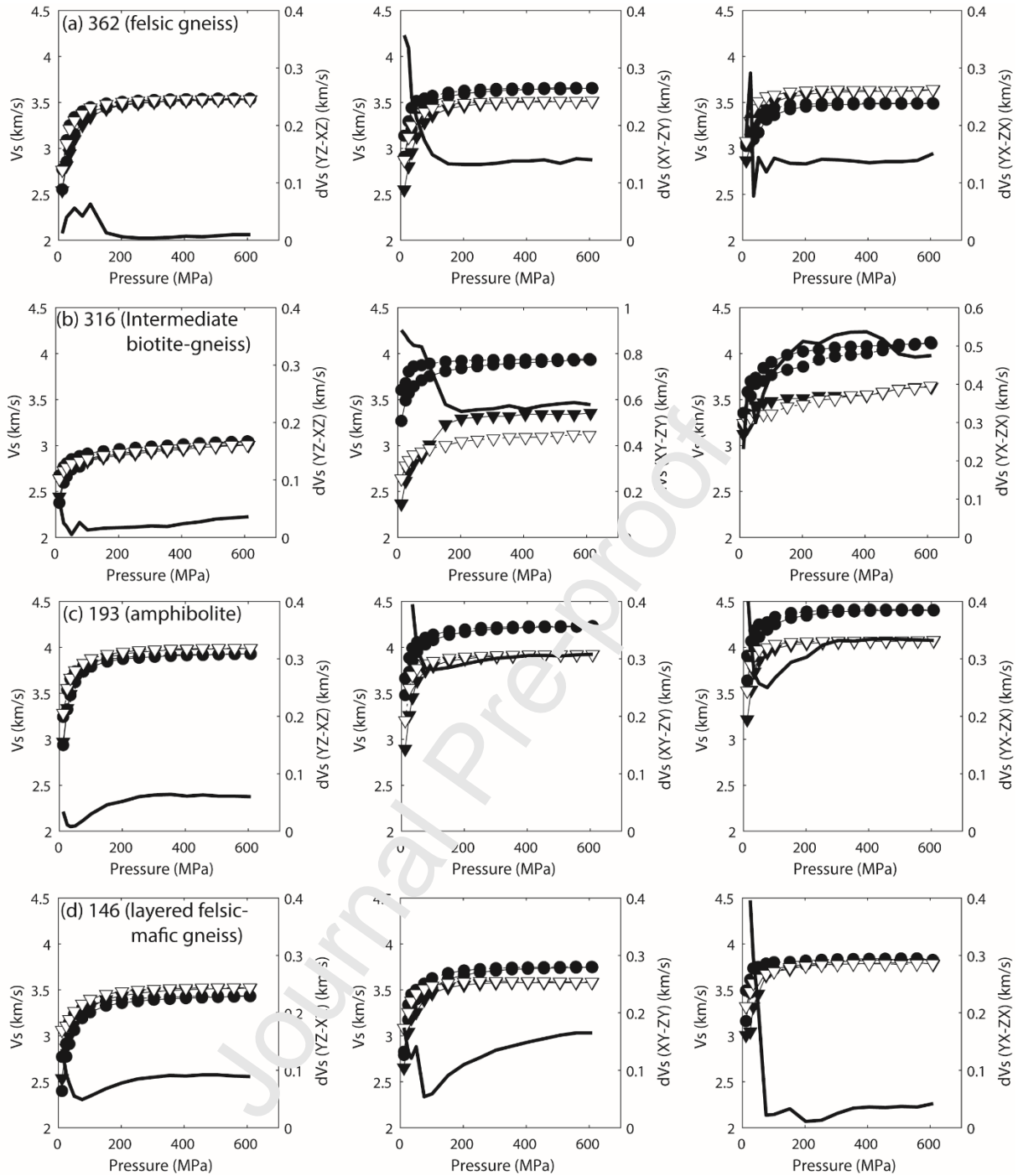


Figure 6: Shear wave velocities and shear wave splitting (dVs) for selected, representative samples (a) 362 – felsic gneiss; (b) 316 – Intermediate biotite-gneiss; (c) 193 – amphibolite; (d) 146 – layered felsic-mafic gneiss. Measurements were carried out at room temperature as a function of pressure. The filled circles show  $V_s$  during pressurization and the open circles represent  $V_s$  during depressurization. The black lines indicate the shear wave splitting value (dVs) for polarized shear waves, as a function of pressure and is read on the right y-axis.

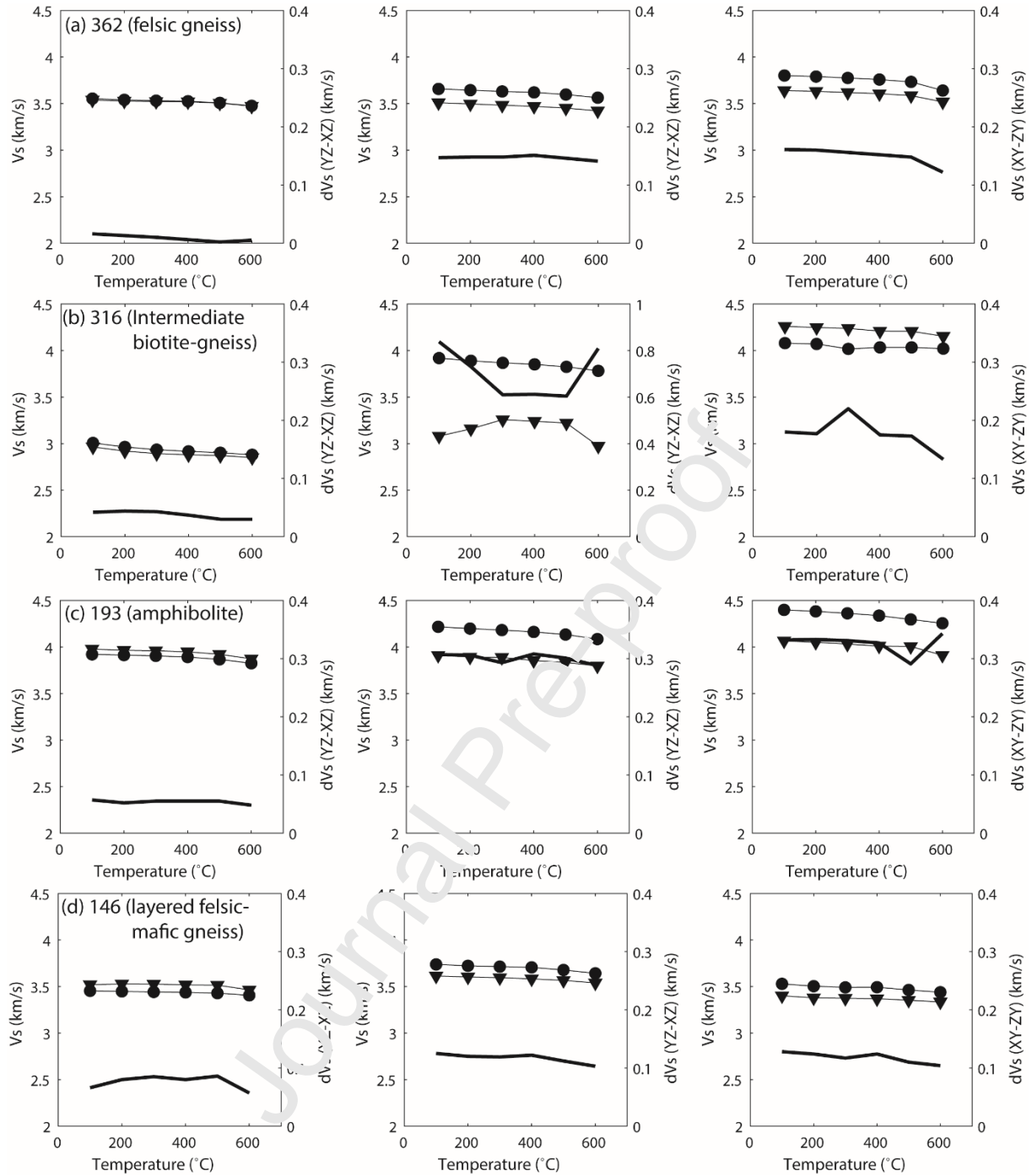


Figure 7: Shear wave velocities and shear wave splitting (dVs) as a function of temperature for samples (a) 362 – felsic gneiss; (b) 316 – Intermediate biotite-gneiss; (c) 193 – amphibolite; (d) 146 – layered felsic-mafic gneiss. Measurements were performed at 600 MPa confining pressure. The black lines indicate the shear wave splitting value (dVs) for polarized shear waves, as a function of temperature and is read on the right y-axis.

#### 4.2 Magnetic Mineral composition and Anisotropy of Magnetic Susceptibility (AMS)

Based on thermomagnetic analyses (online supplementary material, S1) and mean susceptibility values, all samples show the presence of ferromagnetic minerals (e.g., magnetite, pyrrhotite, hematite), although in varying amounts. The analysis is done in order to identify if potential

ferromagnetic minerals, in addition to Fe-bearing paramagnetic (matrix) phases (such as amphibole and biotite), can be contributors to the AMS. Sample 248 shows significant ferromagnetic minerals, based on bulk susceptibility (Fig. 8a, b) and thermomagnetic analysis. Six out of eight samples show a decrease in susceptibility as a function of temperature around 300-320 °C suggesting the presence of pyrrhotite or possibly conversion of maghemite, which is unstable at higher temperatures (Fig. S1). Seven out of the eight samples show a susceptibility drop at ~580 °C, which indicates magnetite is present.

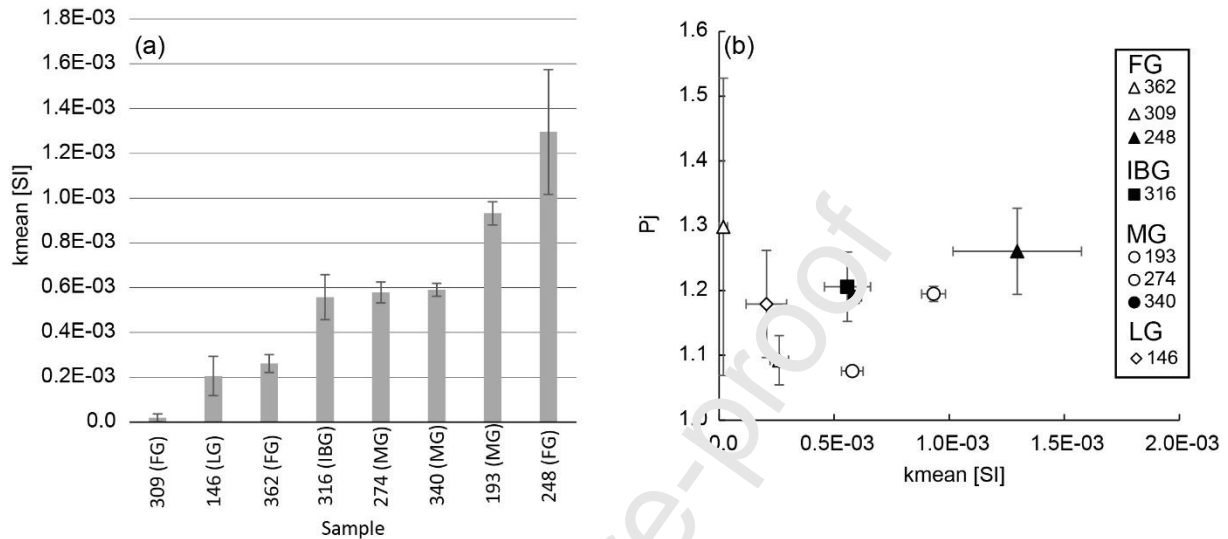


Figure 8: Mean susceptibility of 63 specimens cut out of the eight cubic samples. a) mean susceptibility against the degree of anisotropy,  $k_{mean}$ . The error bars represent two standard deviations and were obtained from the measurements of the AMS sub-samples. b) mean susceptibility for each sample with two standard deviations (obtained from measurement of the AMS sub-samples).

For all samples, the  $k_{min}$  axis plots sub-parallel to the pole to foliation (Fig. 9; Z sample axis). The  $k_{min}$  axis is less well grouped for samples 248 and 309 (felsic gneisses) and deviates somewhat from the pole to foliation.  $k_{max}$  and  $k_{int}$  axes plot in the X-Y plane, and are typically clustered. Although the mineral lineation is marked by the sample X-axis, there is not an apparent consistent relationship between the  $k_{max}$ -axis and X-axis. A few samples display  $k_{max}$  being sub-parallel to the X-axis, including 274 (mafic gneiss), 309 (felsic gneiss) and 316 (intermediate biotite-gneiss), whereas other samples show  $k_{max}$  sub-perpendicular to the lineation, such as 146 (layered felsic-mafic gneiss), 193 (mafic gneiss), and 248 (felsic gneiss). Samples 274 (amphibolite) and 362 (felsic gneiss) show  $k_{max}$  between the X- and Y-axes.



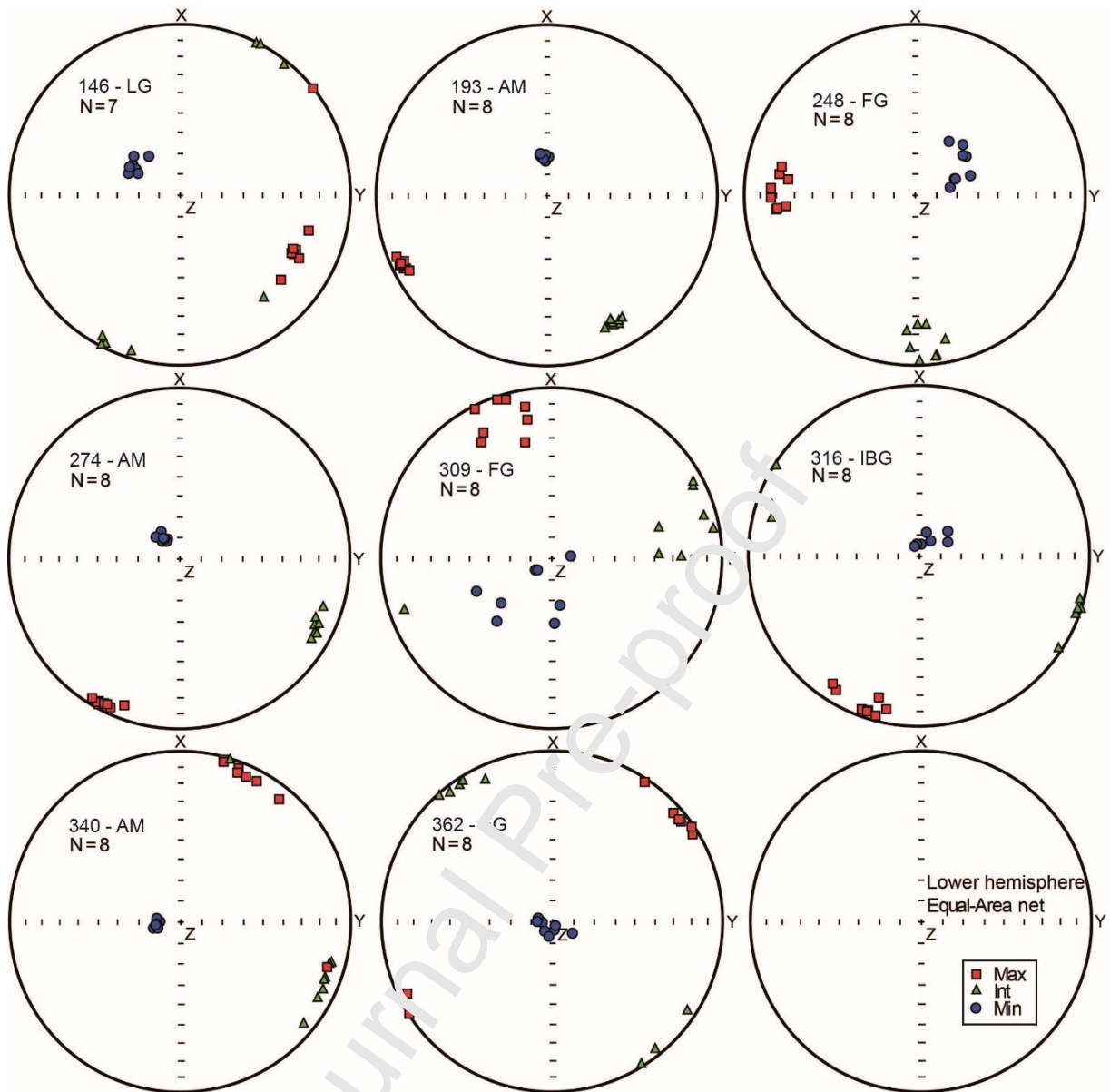


Figure 9: Anisotropy of magnetic susceptibility plotted in lower hemisphere equal area nets for subsamples (N) of the original cubes used for ultrasonic velocity experiments. X, Y and Z axes correspond to the sample reference frame used for the ultrasonic measurements. Abbreviations in the figure are provided in the sample description are FG: gneiss; IBG: intermediate biotite gneiss; LG: layered gneiss; AM – amphibolite.

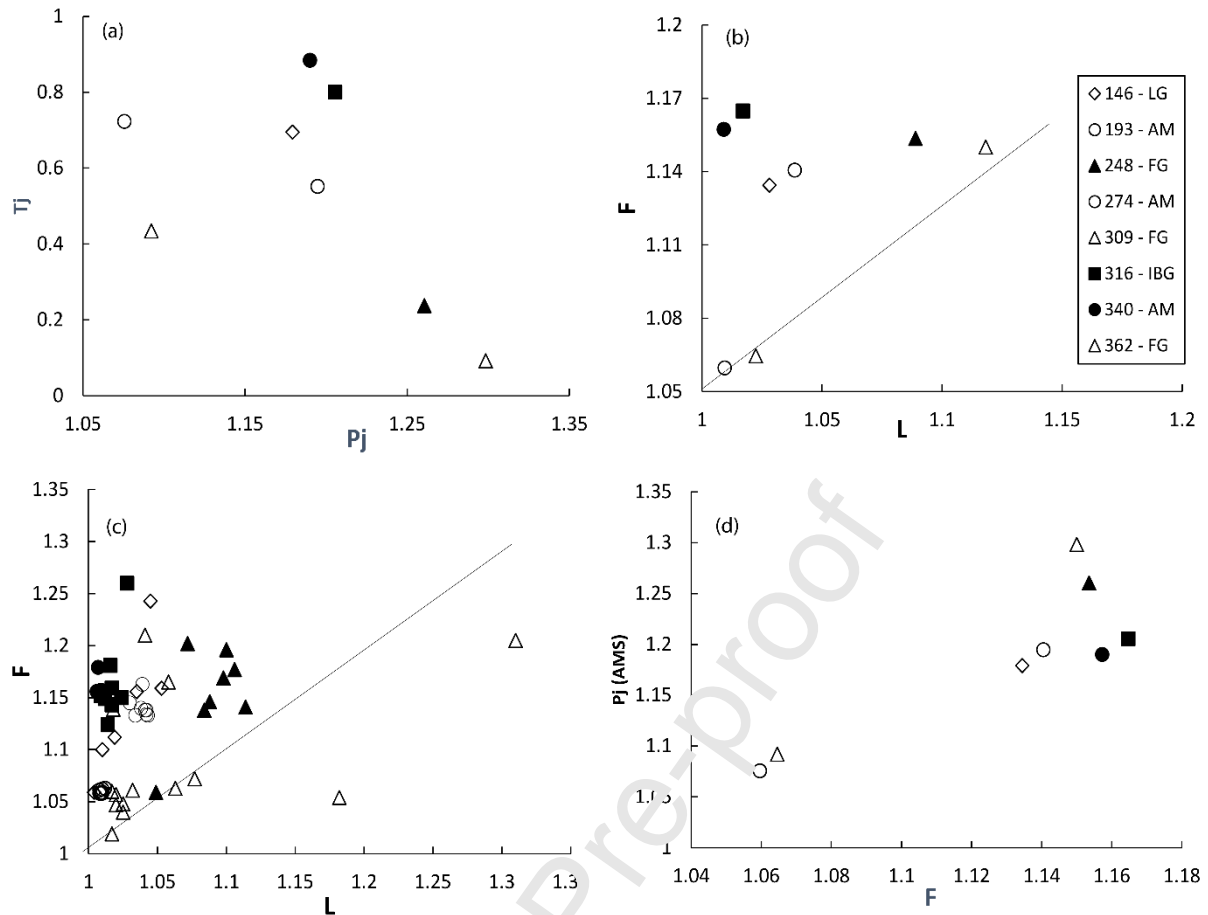


Figure 10: Anisotropy of magnetic susceptibility parameters,  $P_j$ ,  $T_j$ ,  $L$  and  $F$ , shown against each other; a) Shape of the anisotropy ( $T_j$ ) vs. the degree of anisotropy ( $P_j$ ); b) mean value of foliation and lineation of all samples and c) magnetic foliation ( $F$ ) and lineation ( $L$ ); d) magnetic foliation to the degree of the anisotropy. The data plotted in (a), (b) and (d) represent the average value based on the set of sub-samples from each cubic sample used for ultrasonic measurements.

Further information regarding the petrofabric, using AMS, can be obtained from plots of the degree of anisotropy, shape parameter and the magnetic lineation and foliation (Fig. 10). Between them, there are six samples showing a foliation dominated AMS, and two samples that show a neutral triaxial magnetic fabric. Samples 274 (amphibolite) and 362 (felsic gneiss) are close to the neutral line (where  $L$  and  $F$  are equal). Samples 309 and 248 (felsic gneisses) plot differently compared to other samples (Fig. 10a), with a  $P_j > 1.25$  and  $T_j < 0.2$ .

Table 2: Compilation ultrasonic wave speed measurements at 600 MPa.  $V_p$  is reported with respect to X, Y and Z axes, and  $V_s$  with respect to the polarization direction. The right-most columns show the linear strain (%) of the samples, comparing room conditions with pressure of 600 MPa.

Sample Name	Density (g/cm³)	Vp (km/s)				A-Vp (%)	Vs (km/s)						A-Vs (%)	ε			
		x	y	z	mean		yx	zx	xy	zy	yz	xz		mean	x	y	z
Felsic gneiss																	
248	2.746	6.561	6.447	6.213	6.407	5.439	3.675	3.556	3.554	3.455	3.478	3.485	3.534	6.241	0.854	0.759	0.918
309	2.654	6.227	6.321	5.996	6.181	5.246	3.791	3.639	3.633	3.636	3.662	3.509	3.645	7.719	0.483	0.536	0.655
362	2.832	6.637	6.518	6.272	6.476	5.630	3.487	3.638	3.654	3.513	3.539	3.529	3.560	4.683	0.390	0.427	0.602
Intermediate Bt gneiss																	
316	3.027	7.011	6.597	5.740	6.449	19.704	4.111	3.636	3.931	3.353	3.039	3.003	3.512	31.550	0.568	0.805	1.270
Mafic gneiss																	
193	3.049	7.474	7.111	6.610	7.065	12.218	4.402	4.070	4.228	3.921	3.928	3.988	4.089	11.760	0.166	0.275	0.463
274	3.040	7.325	6.652	6.713	6.897	9.759	4.225	4.033	4.096	3.875	3.892	3.906	4.005	8.761	0.298	0.382	0.520
340	3.041	7.587	7.233	6.325	7.049	17.905	4.447	3.710	4.241	3.609	3.640	3.632	3.880	21.601	0.326	0.334	0.710
Layered felsic-mafic gneiss																	
146	2.787	6.480	6.263	5.928	6.224	8.870	3.820	3.778	3.747	3.532	3.431	3.520	3.646	10.663	0.430	0.492	0.743

Table 3: Compilation of data from ultrasonic laboratory experiments at 600 °C and 600 MPa. Vp is reported with respect to X, Y and Z axes, and Vs with respect to the polarization direction. The right-most three columns show the linear strain (%) of the samples, comparing room conditions with pressure and temperature of 600 MPa and 600 °C.

Sample Name	Density (g/cm <sup>3</sup> )	Vp (km/s)			A-Vp (%)	Vs (km/s)						A-Vs (%)	ε				
		x	y	z		mean	yx	zx	xy	zy	yz		xz	mean	x	y	z
Felsic gneiss																	
248	2.714	6.262	6.095	5.907	6.088	5.335	3.341	3.334	3.371	3.262	3.485	3.349	3.357	6.651	0.949	0.928	1.180
309	2.602	6.042	6.077	5.799	5.973	4.661	3.583	3.550	3.553	3.556	3.772	3.662	3.613	6.148	0.376	0.464	0.611
362	2.795	6.490	6.327	6.072	6.290	6.472	3.473	3.468	3.559	3.419	3.635	3.513	3.511	6.160	0.356	0.457	0.624
Intermediate Bt-gneiss																	
316	2.964	7.008	6.452	5.503	6.321	23.805	2.880	2.850	3.782	2.973	4.021	4.154	3.443	37.869	0.411	0.747	1.204
Mafic gneiss																	
193	2.992	7.357	6.879	6.422	6.906	13.545	4.255	3.912	4.085	3.797	3.825	3.873	3.958	11.577	0.177	0.293	0.477
274	2.988	7.213	6.940	6.521	6.891	10.034	3.790	3.809	3.834	3.730	4.112	3.871	3.858	9.901	0.194	0.351	0.507
340	2.980	7.535	7.073	6.116	6.908	20.546	3.531	3.527	4.109	3.472	4.320	3.598	3.760	22.568	0.199	0.265	0.673
Layered felsic-mafic gneiss																	
146	2.735	6.336	6.068	5.725	6.043	10.117	3.406	3.464	3.642	3.539	3.439	3.335	3.471	8.853	0.388	0.466	0.674

## 5. Discussion

### 5.1. Influence of pressure, temperature and microcracks on seismic anisotropy

There are several possible sources for the generation of seismic anisotropy, most notably the existence of microcracks, crystallographic preferred orientation (CPO) and shape preferred orientation (SPO), as well as layering and compositional banding of minerals and rocks (Babuska and Cara, 1991). The exponential increase in Vp as a function of pressure in Figures 5 and 7 represent the zone of crack closure pressure, which ranges from up to 150 MPa to 350 MPa, in line with observations reported by Ji et al. (2007) and Sun et al. (2012) for drill core samples. Generally, microcracks are prone to close at confining pressures exceeding 100-200 MPa (Kern et al., 1997; Kern

et al., 1990). The closure pressure varies somewhat for each sample, but typically the relationship between  $V_p$  and  $V_s$  as a function of pressure tends to become linear above 200 MPa (Figs. 5, 7). Additionally, the velocity as a function of crack closure pressure varies depending on the direction of measurement. Compare, for example,  $V_p$  as a function of pressure along X and Z axes in Figure 5 (a, b; felsic gneiss 362 and intermediate biotite gneiss 316), which show markedly different pressurization and de-pressurization curves along the two axes. During depressurization, the cracks gradually re-open, although not to the same extent as before pressurization, resulting in hysteresis (Ji et al., 2007). The experimental data show that this hysteresis effect is largest along the Z-axis (Fig. 5), which is the axis that is normal to the orientation of the foliation plane, suggesting that this plane exhibits the largest amount of interaction with microcracks; i.e., microcracks tend to orient parallel to the foliation plane. Similar effects were observed during the temperature increase (Figs. 6 and 8), indicating that at higher temperature microcracks appear to be generated and thus reduces  $V_p$  and  $V_s$ .

To further assess the different loading and unloading effects we plot  $V_p$  variations along different sample axes, e.g.,  $V_p(X)-V_p(Z)$ , during pressurization to 600 MPa and depressurization to room pressure (Fig. 12). This projection of data is useful to show the development of sample anisotropy, comparing different sample axes, as a function of pressure (hence reflecting micro-crack closure as a function of pressurization and depressurization). Notably, the intermediate biotite gneiss (Fig. 12b) stands out among the tested samples as it does not show a reversible path for  $V_p$  during pressurization and depressurization. For this sample, the difference between  $V_p$  along X, Y and Z axes remain similar upon depressurization, which most likely indicates that micro-cracks do not re-open during depressurization.

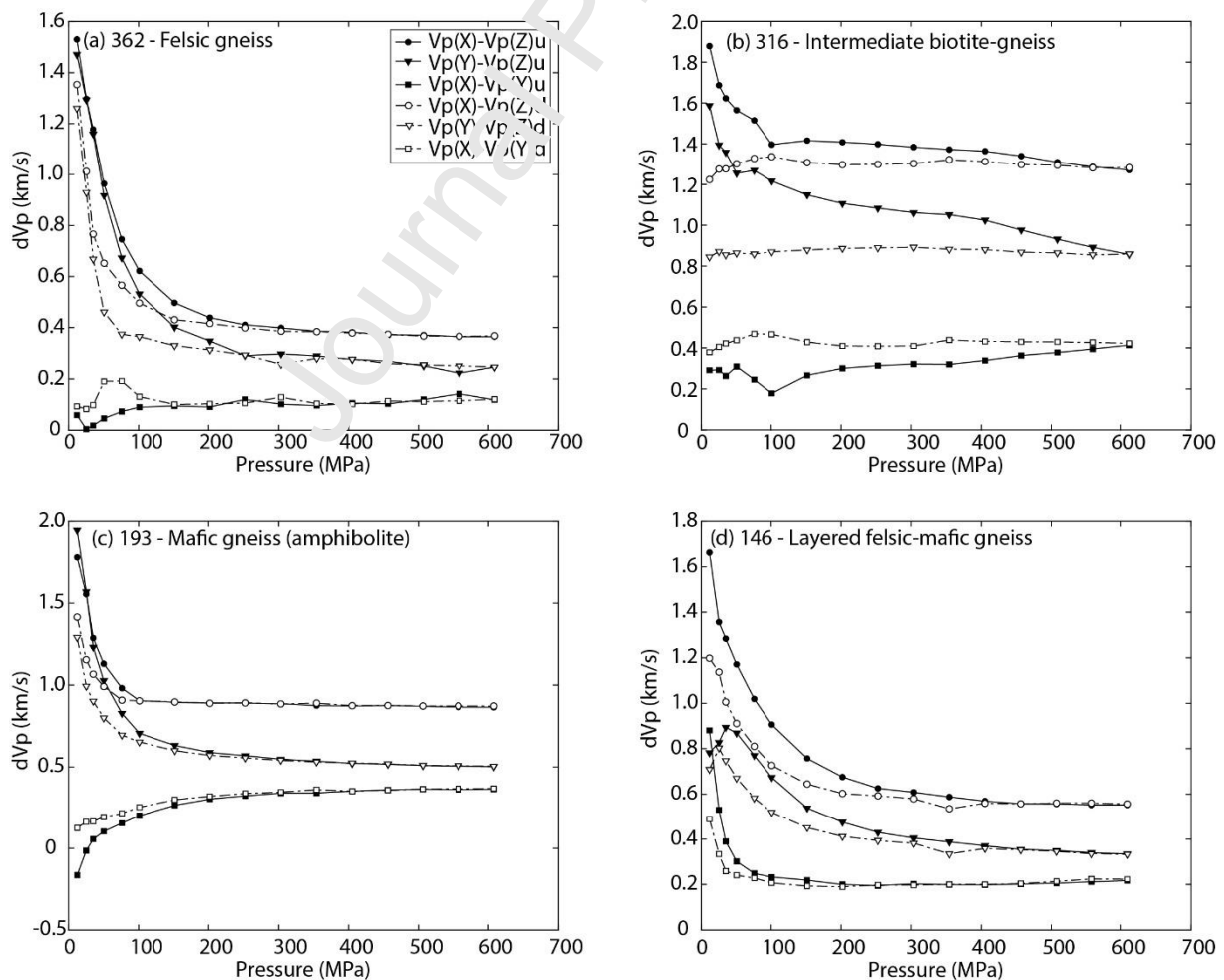


Figure 11. Differences in Vp along different sample directions, expressed by Vp(X)-Vp(Z), Vp(Y)-Vp(Z) and Vp(X)-Vp(Y), for samples (a) 362 (Felsic gneiss), (b) 316 (intermediate biotite-gneiss), (c) 193 (amphibolite) and (d) 146 (layered felsic-mafic gneiss). The letter 'u' and 'd' in the legend indicates pressurization and depressurization, respectively.

All samples were re-measured at room pressure and room temperature the day following the pressurization and depressurization experiment (i.e., the sample was allowed to remain in the pressure vessel at ambient pressure conditions), to investigate possible effects of residual stresses. Although not shown in a figure, samples showed that they had accumulated residual stresses having only partially released the stress the day after the loading measurement. The difference between Vp measurements before and after the pressure cycling ranged from 5 % to 20 %, depending on the sample, which we believe is the result of closure (and slow re-opening) of pre-existing intercrystalline cracks since we did not observe any localized damage or deformation in the thin sections (e.g., Figs. 3 and 4; note that thin sections were prepared from the sample cube subsequent to the ultrasonic measurements). However, for all samples, the largest differences were observed normal to the foliation.

With an increase in pressure from room conditions to 600 MPa, there is a successive diminishing in P- and S- wave anisotropy (Fig. 5). However, when pressure remains fixed at 600 MPa and temperature increases from room conditions to 600 °C, the P-wave anisotropy increases by up to 4 % from its value at 600 MPa and room temperature (e.g., Fig. 6b). This observation is similar to the trend observed during depressurization, suggesting that changes in anisotropy are due to the reopening of intercrystalline cracks. The increase in AVp by applying temperature ranges from 0.4 % in sample 248 (felsic gneiss) up to 4 % in sample 316 (intermediate biotite gneiss; Fig. 6). Anisotropy of P- and S-wave velocities increases to a greater extent in amphibolites compared to the layered sample (146) and felsic gneisses, as a function of temperature. The layered sample 146 (layered felsic-mafic gneiss) follows a similar trend of AVp as a function of temperature as other samples (in particular amphibolites). At 600 MPa, this sample has a relatively high AVp = 8.9 %, and AVp increases to 10.1 % as a function of pressure and temperature (at 600 MPa and 600 °C). This may indicate that thermal expansion, or the temperature dependence of Vp and Vs, of different minerals, plays a significant role in increasing AVp and AVs. One possibility is that the directional dependence of thermal expansion in amphibole (Tirhaudino et al., 2008) can affect the anisotropy of elastic wave measurements. Also, the anisotropic thermal expansion of biotite seems to be one of the most logical reasons for an increase in seismic anisotropy as a function of temperature for samples 316 (intermediate biotite gneiss) and 340 (biotite-bearing amphibolite). Siegesmund et al. (2008) has noted the considerable difference of thermal expansion along the c-axis ( $\alpha = 17.3 \times 10^{-6} \text{ K}^{-1}$ ) and within the basal plane ( $\alpha = 9.65 \times 10^{-6} \text{ K}^{-1}$ ). This difference, of nearly two times higher expansion along the c-axis, may be of importance also in influencing seismic anisotropy (at least on a laboratory scale). Notably, samples 309 (felsic gneiss), and 193 (amphibolite) showed a reduction of AVs during temperature-dependent measurements, compared to measurements made solely at confining pressure, and thus deviate from the trend exhibited by other samples.

Samples 316 and 340 contain a significant amount of biotite (>10 %), with an AVp of 19.7% and 17.9%. Although sample 340 is dominated by amphibole, the observed AVp is high considering the high single-crystal AVp (up to 27 %) of amphibole (hornblende; Aleksandrov and Ryzhova, 1961; Aleksandrov et al., 1974; Brown et al., 2016), together with the additional influence of biotite. Biotite has very high single-crystal anisotropy, with AVp ~64 % (Aleksandrov and Ryzhova, 1961). Qualitatively, SPO of biotite is apparent for both samples 316 and 340 (e.g., Fig. 3d), which is likely to coincide with the CPO and hence produce a high seismic anisotropy.

## 5.2. Application of COSC-1 sample results to seismic anisotropy of the middle to lower continental crust

### 5.2.1 Elastic wave speeds from COSC-1 laboratory studies

Two other laboratory studies have presented data on elastic wave velocity and anisotropy from the COSC-1 project (Wenning, et al. 2016; Kästner et al., 2020). These previous studies used three one-inch diameter bored plugs from each drill core sample; each plug was taken along a different axis, representing the structural X, Y and Z axes, from which elastic wave anisotropy could be calculated. Wenning et al. (2016) provided AVp, AVs and calculated Thomsen parameters, at confining pressures up to 260 MPa. Kästner et al. (2020) provided p-wave velocities of sixteen core samples with measurements made up to 250 MPa confining pressure and compared the results with on-drillcore Vp measurements at ambient conditions and borehole sonic logging data. The present work extends these conditions by measurements up to 600 MPa and additionally adding temperature-dependent measurements, up to 600 °C. A comparison of data obtained from the three studies is given in Figures 12 and 13. AVp (%) vs AVs (%) data and a comparison of calculated Thomsen parameters are given in Figure 12a, b (only based on Wenning et al., 2016 and this study). There is a fair agreement between AVp and AVs (Fig. 12a), even though the peak confining pressures are rather different (comparing 260 MPa and 600 MPa). Note that the anisotropy that was obtained at 600 MPa in this study, is compared with the crack-free back-extrapolated anisotropy (labelled AVp<sub>0</sub>; AVs<sub>0</sub>), which was calculated by Wenning et al. (2016) and Kästner et al. (2020) (Figs. 12 and 13). For the Thomsen parameters, there is relatively little change in  $\gamma$ , and values typically range up to 0.06 (sample 316, intermediate biotite gneiss, shows a deviation with  $\gamma \sim 0.15$ ), while there is a larger range in  $\epsilon$ . This is due to the smaller differences between the fastest and slowest S-wave velocities, which influences  $\gamma$ . In comparison, there are relatively larger differences in Vp among samples, leading to a wider range in  $\epsilon$ .

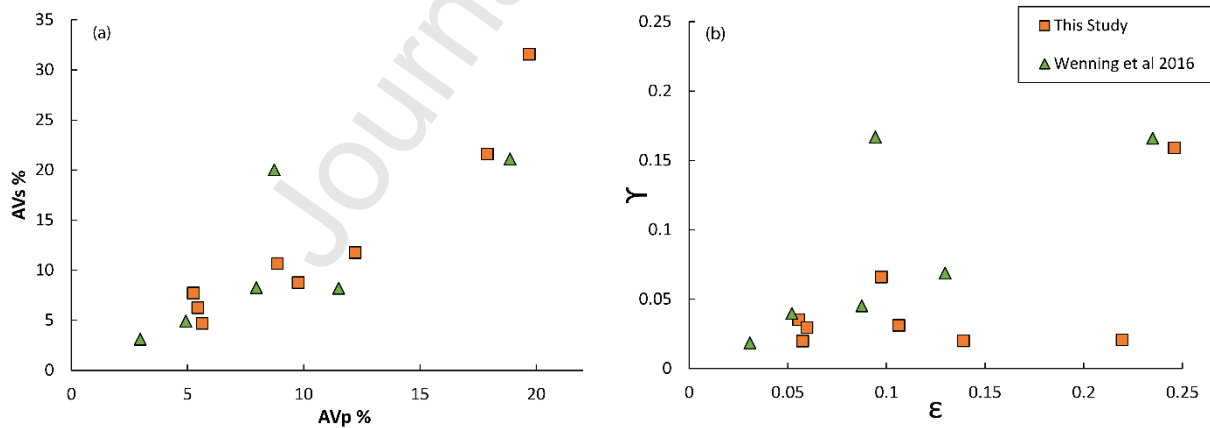


Figure 12: Elastic wave parameters calculated from ultrasonic wave propagation data. These values are calculated directly from elastic wave speed and density results. a) Percentages of AVp (%) and AVs (%) plotted against each other (data from this study and Wenning et al., 2016). b) Relationship between Thomsen parameters ( $\epsilon$  and  $\gamma$ ), (data from this study and Wenning et al., 2016). Wenning et al. (2016) carried out measurements up to 260 MPa confining pressure; in this study, the comparable data were measured up to 600 MPa.



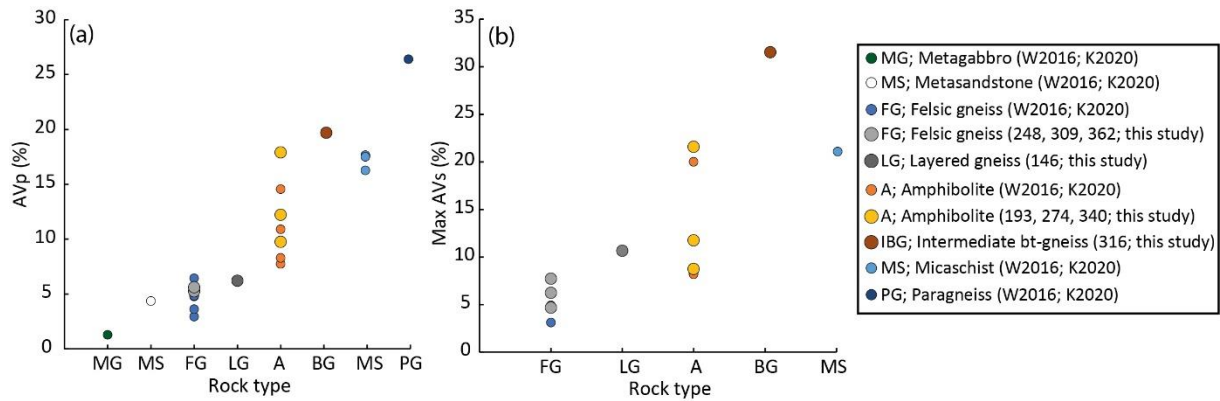


Figure 13: A comparison of (a) AVp and (b) Max AVs from this study and the studies of Wenning et al. (2016) and Kästner et al. (2020). Note the different sizes of the circles, where large circles are from this study and smaller circles are from Wenning et al. (2016) and Kästner et al. (2020).

### 5.2.2 Implications for crustal seismic anisotropy

One of the main aims of the COSC-1 project is to understand how the Middle Allochthon Lower Seve Nappe rocks were emplaced into the middle crust during the Caledonian orogeny (Gee et al., 2010; Gee et al., 2013; Lorenz et al., 2015). The rocks experienced large scale ductile flow during emplacement, at middle crustal conditions to amphibolite prograde metamorphic conditions. The laboratory conditions we apply in this study (600 MPa and 600 °C) appear appropriate to recreate the mid-crustal conditions that these rocks experienced during emplacement (and subsequent to their emplacement), and may therefore be of use when comparing lab results to present-day settings where middle crustal flow currently occur (e.g., Himalaya-Tibet). The results of AVp and AVs for amphibolites and biotite bearing gneiss and amphibolite are generally around 10 % or higher. Felsic gneisses samples are comparatively less anisotropic, with AVp of <7 % and AVs of <6 %. These results share notable similarities with other experimental studies on cubic samples employing multi anvil apparatus to pressures of 600 MPa (e.g., Babuska and Cara, 1991; Barruol et al., 1993; Barruol et al., 1996; Kern et al., 1999; Kern et al., 2002; Kern et al., 2008).

The impact of the results in this study concerns both the intrinsic (i.e., CPO and SPO) and extrinsic sources (i.e., microcracks) of anisotropy. There are several studies on samples at elevated pressure, where the influence of open micro-cracks and pores are gradually reduced (e.g., Wyllie, 1958; Todd and Simmons, 1972; Eberhart-Phillips et al., 1989; Ji et al., 2007; Madonna et al., 2012). It is generally assumed that most microcracks are closed above 200 MPa, which would in nature correspond to a depth of ~7-8 km (Emmermann et al., 1997). However, from the KTB well in Germany, it is known that fluid-filled fractures and pores can remain open until 9 km depth (Kern, et al., 1991). Sun et al. (2012) studied samples collected from the Chinese Continental Scientific Drilling (CCSD) cores and reported that most microcracks were newly formed by the release of in-situ stresses in the borehole. These microcracks are relatively clean without secondary mineral fillings and have smaller aspect ratios, and thus more easily closed under the applied hydrostatic pressure conditions in the laboratory. After the cracks are fully closed, the core samples that contain little weathering products, are much less sensitive to pressure and thus have lower pressure derivatives and smaller hysteresis than the samples collected from the surface outcrops. To understand the effects of cracks better we need to consider their closure pressure carefully. Equations derived by Walsh (1965), based on continuum elasticity theory, indicates that crack-closure is closely related to the shape of the microcrack, and in particular its aspect ratio. Higher aspect ratio cracks, or pores, may remain open

to pressures >1 GPa pressure as experimentally shown by Christensen (1974). In fact, it is impossible to close high aspect ratio pores (i.e., spherical pores) or cracks fully during pressurization (Walsh, 1965). A lower aspect ratio of cracks leads to an increase in rock compressibility, which is reduced during pressurization. Additionally, Walsh (1965) showed that low aspect ratios generally increase elastic anisotropy in rock prior to closure during pressurization. The influence of temperature on the opening of microcracks and elastic anisotropy is nonlinear, considering measurements from room conditions up to 600 °C. There is an apparent reduction in  $V_p$  and  $V_s$ , but a general increase in anisotropy. We can only speculate as to the origin of the increase in seismic anisotropy, but thermal expansion due to alignment (CPO) of the minerals appear as a plausible explanation, as is noted in section 5.1.

Cracks and pore spaces are important sources of anisotropy in the upper crust, but tend to diminish as we move deeper into the crust (Schijns et al., 2012; Audet, 2015). Therefore, it is important to investigate the influence of microcracks versus intrinsic anisotropy. Intrinsic anisotropy does not depend on microcracks but on constituting minerals and the fabric of the rock while extrinsic anisotropy is crack-related. We observed that intrinsic anisotropy is containing 20% to 25% of the initial anisotropy values of biotite gneiss and amphibolite, felsic gneiss and mixed layered samples due to the assumption of microcracks and pores effects diminishes and are negligible by 600 MPa confining pressure. The pressure range of the crack closure in metamorphic rocks has been the subject of investigations in different studies to better understand the middle and lower crust, as well as the upper mantle (Anderson, et al., 1974; Ji et al., 2003; Ji et al., 2007). A general increase in seismic anisotropy is furthermore observed due to the increase in temperature at 600 MPa confining pressure. In our samples, we observed up to 3 to 4 times reduction in anisotropy when comparing ambient and maximum confining laboratory pressure conditions (600 MPa). Additionally, seismic anisotropy generally increased slightly when increasing temperature to 600 °C. The most drastic change in anisotropy occurs for sample S16 (intermediate biotite-gneiss), where  $AV_p$  increases from 19.7 % (at 600 MPa and room temperature) to 23.8 % (at 600 MPa and 600 °C). The origin of the increase in anisotropy results mainly from the linear decrease in  $V_p$  along with the sample Z-axis (normal to foliation) as a function of increasing temperature, whereas  $V_p$  remains more or less unchanged along the sample X-axis (parallel to mineral lineation). Therefore, we suggest that at conditions representative for the middle and lower crust, ~80- to 90% of anisotropy exhibited by the biotite bearing specimens, felsic gneiss and amphibolites are due to intrinsic sources of anisotropy, including CPO and SPO, whereas micro-cracking can still contribute up to 20 % of anisotropy (even at mid-crustal conditions). Clearly, crack and pore space at depth will not be empty or dry, as in experiments performed in this study. The presence of any type of pore fluid is likely to increase the effect of crack or porosity influence on seismic anisotropy since the effective pressure can be reasoned to be lower than the confining pressure. Even if the influence is smaller than at upper-crust levels, the presence of micro-cracks should therefore be considered in observed seismic anisotropy at middle and lower crustal conditions.

### 5.3 Relationship between AMS and elastic wave anisotropy

As derived seismic parameters are in principle analogous to parameters used to describe AMS, it is reasonable to hypothesize that AMS, as a petrofabric indicator, can be used as a proxy for elastic wave anisotropy. However, the latter type of measurement is simplified because it is only represented by measured values along three axes and not the complete elastic tensor. A positive correlation between seismic anisotropy and magnetic susceptibility anisotropy was shown experimentally by Punturo et al. (2017) on metamorphic rocks, although their samples were weakly

anisotropic. In contrast, Biedermann et al. (2020) noted that the relationship between seismic and magnetic anisotropy is not straightforward, given that the former is governed mainly by the bulk mineral composition, whereas the latter is controlled to a great extent by small amounts of ferromagnetic minerals. A complicating factor, observed particularly in shear zones, is the obliquity between the CPO and SPO (Ji et al., 1996). Such obliquity can yield a significant difference between AMS and seismic anisotropy, in particular when bulk magnetic susceptibility exceeds  $1 \times 10^{-3}$  SI, and the magnetic fabric is likely to be controlled by the SPO of ferrimagnetic iron oxides (Rochette et al. 1992).

Here, we discuss the results of the measurements of AMS in comparison with the ultrasonic wave data. The rationale for this approach is that we can use AMS data as a proxy for the petrofabric (CPO and SPO) and link this to elastic wave anisotropy, based on the inference that AMS provides a suitable proxy for SPO and CPO of the major rock-forming minerals (Owens and Rutter, 1978; Punturo et al., 2017). The aim is to provide the conditions for when AMS is a suitable proxy for seismic anisotropy. It has to be acknowledged that magnetic susceptibility and elastic wave velocity values of the minerals are generated partly from the same source, mainly because of the CPO of paramagnetic (matrix) minerals, but also in part from different sources. The magnetic susceptibility and its anisotropy are related to mineral composition and mineral chemistry, whereas elastic wave anisotropy results mainly from CPO (Almqvist et al., 2015; Biedermann et al., 2020). In addition, magnetic susceptibility is strongly influenced by the presence of ferromagnetic minerals, whereas the elastic wave velocities arise mainly from the bulk mineral composition. Lagroix and Borradaile (2000) have noted that mafic silicate rocks mostly have magnetic susceptibility higher than predicted based on their chemical compositions. This is due to magnetite inclusions in the silicate grains, which may also increase the magnetic anisotropy. To illustrate the relationship between AMS and elastic wave anisotropy, Figure 14 shows a comparison of parameters obtained from measurements of AMS and elastic wave velocities.

Mica and amphibole-dominated rocks represent important sources of anisotropy in the deformed middle and lower crust. Between our measured samples, the biotite bearing and amphibole-rich samples clearly have the highest seismic anisotropy at ambient temperature and 600 MPa confining pressure conditions as well as 600 MPa and 600 °C. Although it was not measured directly, this most likely reflects the effect of strong crystallographic preferred orientation, which can be qualitatively inferred from Figure 4 and also Figure 14, for the discussion on the general correlation between AMS and elastic wave anisotropy. Mica and amphibole single crystals also show considerable AMS and importantly their mean susceptibility is in the paramagnetic-dominated susceptibility range and hence their principal axes of susceptibility coincide with the crystallographic axes and CPO of a sample (e.g., Martín-Hernandez and Hirt, 2003; Biedermann et al. 2015; Biedermann, 2018). In the case of mica, including biotite and muscovite, there is a relatively straightforward relationship between the principal axes of susceptibility and the crystallographic axes. The  $k_1$  and  $k_2$  axes are oriented within the basal plane of the mica, which hosts the  $a[100]$ - and  $b[010]$ - crystallographic axes, whereas the minimum susceptibility ( $k_3$ ) is oriented normal to the basal plane, along the  $c$ -axis  $[001]$ . This petrofabric and AMS relationship makes it simple to compare with seismic anisotropy since there is an apparent direct agreement between physical properties and crystallography. Amphibole, in contrast, is more challenging to directly relate AMS and seismic anisotropy, because the highest susceptibility ( $k_1$ ) and highest elastic stiffness (e.g.,  $c_{11}$ ) may not coincide. AMS in single-crystal amphiboles mainly depends on the chemical composition and location of the iron the amphibole (Biedermann, 2018). In addition, the problem with inclusions of iron-oxides within dia- and paramagnetic silicate grains will affect AMS (Lagroix and Borradaile, 2001; Feinberg et al., 2006),

although with negligible influence on seismic anisotropy. The approach of using AMS as a proxy for seismic anisotropy must therefore be made cautiously, even in the qualitative case.

Figure 14(a,c) shows the relationship between the degree of magnetic anisotropy and seismic anisotropy. Among the eight samples, six shows a moderate linear relationship between the degree of magnetic anisotropy [ $P_j$  (AMS)] and anisotropy of ultrasonic waves ( $AV_p$  and  $AV_s$ ). The  $P_j$  (AMS) correlate better with  $P_j(V_p)$  than  $P_j(V_s)$ . Between our samples, the best fits are recognized for the biotite bearing and amphibole-rich samples, 316 and 340 (Fig. 14a, c). Samples 248 and 309 do not follow the linear relationship and show lower seismic anisotropy, making it challenging to directly compare their AMS and seismic anisotropy (Figure 14a, c). Based on the thermomagnetic curves (online supplementary material) it is observed that samples 248 contain magnetite (and other potential ferromagnetic minerals). Magnetite is very magnetic and even a small modal proportion ( $<<1\%$ ) can dominate the magnetic susceptibility of rock; a fraction of magnetite can change the AMS by changing the shape ( $T_j$ ) and degree of anisotropy ( $P_j$ ) (Rochette et al., 1992). Such a small amount of magnetite will not influence the ultrasonic wave velocity; although it is very influential with regard to magnetic susceptibility. In contrast, sample 309 (felsic gneiss) shows a mean susceptibility that is close to zero (Fig. 9a, b). The high degree of anisotropy is a result of the low mean susceptibility (close to zero), and not the rocks' inherent magnetic anisotropy (Hrouda, 1986; 2004). The layered Felsic-mafic gneiss (sample 146) lies between the mafic and felsic gneiss samples.

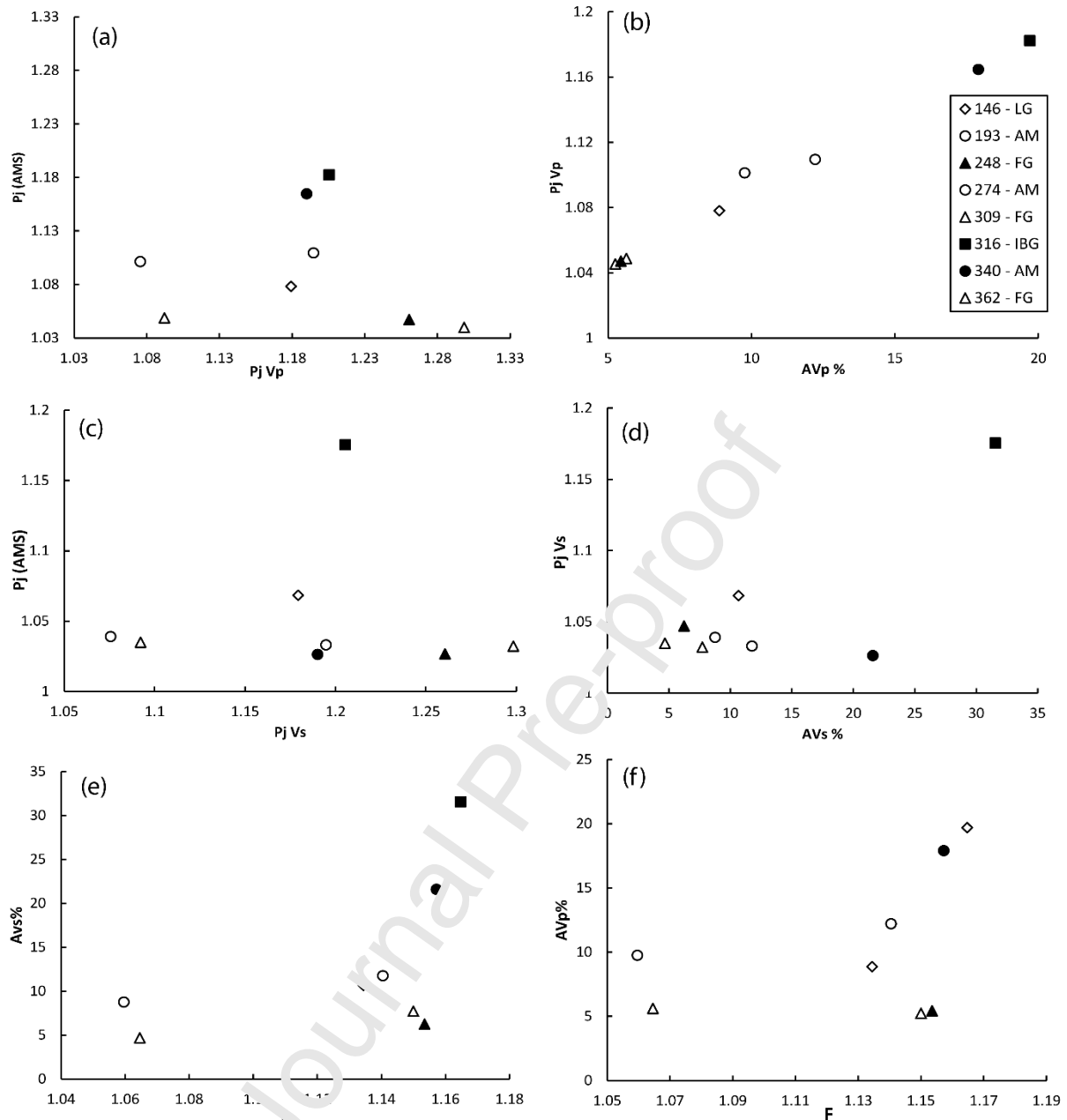


Figure 14: A comparison of seismic anisotropy with magnetic susceptibility. a) degree of anisotropy of magnetic susceptibility compared to the degree of anisotropy of compressional wave anisotropy; b) degree of anisotropy of  $V_p$  compared to  $AV_p$ ; c) degree of anisotropy of magnetic susceptibility compared to the degree of anisotropy of shear wave anisotropy; d) degree of anisotropy of  $V_s$  compared to  $AV_s$ ; e)  $AV_s$  as a function of magnetic foliation; f)  $AV_p$  as a function of magnetic foliation.

To assess if the degree of anisotropy of the fabric directly influences the nature of the anisotropy of magnetic susceptibility, we do the following: 1) calculate the “foliation” of magnetic susceptibility (eq. 10); 2) plot the magnetic foliation relative to elastic wave anisotropy ( $AV_p\%$ ,  $AV_s\%$ ; Fig. 14e, f). P wave velocity data indicate a more linear relation, and straight-forward relationship, with AMS among samples in this study compared shear wave velocity measurements. The additional solutions available for the splitting of shear waves along the three sample axes is likely adding to the complexity of relating  $AV_s$  to AMS.

With this study, we show that there is a relation between AMS and seismic anisotropy. However, this relation can be affected significantly by highly (Ferro)magnetic minerals or a mean magnetic susceptibility close to zero. The existence of these highly magnetic minerals significantly increases the mean susceptibility and the absence of paramagnetic minerals. These effects cannot be seen in the ultrasonic data during laboratory measurements, simply because these highly magnetic minerals are not present in large enough volume to affect the elastic wave velocities. Additionally, a combination of paramagnetic and diamagnetic minerals can lead to a susceptibility close to 0 [SI]. A rock that consists of such a combination of minerals, with mean magnetic susceptibility close to zero, is not suitable as a proxy for seismic anisotropy. Samples that contain ferromagnetic minerals with mean susceptibility between  $2\text{e-}3$  and  $10\text{e-}3$  SI appear to be the most suitable samples to study the seismic anisotropy and AMS relationship, giving rise to a relatively linear relation between  $\Delta V_p$  and the degree of magnetic anisotropy ( $P_j$ ). However, caution is needed when relating the orientation of principal axes of susceptibility and orientation of maximum and minimum  $V_p$ .

It should be noted that there is a systematic challenge in comparing AMS with elastic wave speed data as AMS has a large range of values (varying over several orders of magnitude) compared with the range of elastic wave velocities which ranges well within one order of magnitude; consequently. Any observed trends are thus tentative, although potential exists with careful analysis to correlate AMS and seismic anisotropy through the petrofabric.

Figure 15 shows a flow chart that aims to indicate how seismic anisotropy (and elastic constants) relate to magnetic susceptibility and the principal axes of susceptibility. Note that this diagram presents the case for selected minerals in the crust, and not an exhaustive attempt to relate seismic anisotropy and AMS for all minerals. It serves with the aim to illustrate what needs to be taken into consideration when making a comparison between seismic anisotropy and AMS. In some cases, the relationship between the two physical properties is straightforward, such as for phyllosilicate dominated rocks, where maximum axes of  $\chi$  and  $k$  coincide. Provided that such rocks are governed by the matrix minerals (paramagnetic and diamagnetic cases), there should also be a reasonable relationship between the degree of anisotropy, as both properties are governed by CPO. The relationship breaks down for cases when susceptibility is close to 0 [SI], as the calculation of  $P_j$  results in artificially high values. In addition, for strongly magnetic rocks, where  $k_{\text{mean}} > 1 \times 10^{-3}$  [SI], it is likely that the ferromagnetic mineral fraction will overtake the contribution to AMS, making a direct comparison between AMS and seismic anisotropy difficult. A qualitative relationship may still exist, however, if there is a coincidence between the SPO (magnetite) / CPO (hematite, pyrrhotite) of the ferromagnetic phases compared to the matrix phases that control seismic anisotropy.







Figure 15. A flow chart that shows how seismic anisotropy (and elastic constants) relate to mean susceptibility ( $k_{\text{mean}}$ ) and anisotropy of magnetic susceptibility. The division is made between samples based on initial mean magnetic susceptibility, with categories for  $<0$  [SI] (diamagnetic dominated rocks),  $\sim 0$  [SI] competing for diamagnetic and paramagnetic mineral fractions in a rock,  $>1 \times 10^{-5}$  SI to  $1 \times 10^{-3}$  [SI] paramagnetic dominated rocks and  $>1 \times 10^{-3}$  [SI], ferromagnetic dominated rocks. Common minerals within each category are shown with indications for maximum, intermediate and minimum axes of Vp and susceptibility (k), with respect to the crystal habit and crystallographic axes of the minerals. Note that principal axes of susceptibility order according to size, such that  $k_{\text{max}} \geq k_{\text{int}} \geq k_{\text{min}}$ , whereas the same is not the case for elastic constants ( $c_{11}$ ,  $c_{22}$ ,  $c_{33}$ ). In the latter case  $Vp_{\text{max}}$ ,  $Vp_{\text{int}}$  and  $Vp_{\text{min}}$  are oriented with respect to the highest, intermediate and minimum elastic constant for a specified mineral. Note that the data for the principal axes of susceptibility were obtained from Biedermann (2018). Elastic constant data for the different minerals are from the following references: amphibole (Brown et al., 2016), orthopyroxene (Chai et al., 1997), diopside (Isaak et al., 2006), biotite (Aleksandrov and Ryzhova, 1961), augite (Aleksandrov et al., 1974), muscovite (Vaughan and Guggenheim, 1986), feldspar (Brown et al., 2016; Vaesermann et al., 2016),  $\alpha$ -quartz (Ohno et al., 2006), olivine (Abramson et al., 1997), calcite (Chen et al., 2001). Parts of this diagram were modified from Biedermann (2018). The boundary used to indicate the paramagnetic dominated region versus the ferromagnetic dominated region is from Rochette et al. (1992).

When the magnetic susceptibility is dominated by matrix minerals, such as in the diamagnetic and paramagnetic cases in Figure 16, it is necessary to consider 1) the magnitude or degree of anisotropy and 2) the directional relationship between principal axes of k and Vp. In regards to the magnitude of anisotropy, there should be a good relationship between seismic and magnetic anisotropy, regardless of the orientation of the principal axes, since it is only the strength of the petrofabric (CPO in this case) that is of relevance. However, in regards to the orientation of the principal axes of seismic and magnetic anisotropy, the relationship is considerably more complicated (Fig. 15). For instance, as noted above, the principal axes agree well in regards to direction in rocks dominated by phyllosilicates. In contrast, the principal axes in amphibole dominated rocks show a complicated relationship, with many possibilities for orientation of the principal axes of magnetic susceptibility (even though the elastic constants show regular directional properties). This is likely the reason why we observe a good relationship between the degree of susceptibility anisotropy ( $P_j$ ) and AVp (%) (Fig. 14a, with exception of felsic gneiss samples 248 and 309), but a more unclear relationship between principal axes of Vp and k (Fig. 10).

## 6. Conclusion

We conducted laboratory measurements to investigate the effects of pressure and temperature on ultrasonic Vp and Vs for amphibolite and gneisses, which are representative of a middle crustal orogenic setting. AMS measurements were made on the same samples to evaluate the relation between AMS and seismic anisotropy. The results and points in the discussion are summarized in the following remarks:

- Results in this study illustrate how micro-cracks affect the (elastic) deformation of samples as well as enhancing anisotropy at pressures from ambient condition to 600 MPa and temperature from ambient conditions to 600 °C. Therefore, laboratory wave velocities measured at confining pressures below 200 MPa may be significantly influenced by microcracks. However, even above 200 MPa, there is likely a contribution of microcracks to elastic anisotropy. In particular, when temperature matches confining pressure (i.e.,  $\sim 1$  MPa

/1 °C), there could be a considerable influence of microcracks on seismic anisotropy, up to 20 % at mid-crustal conditions (600 MPa and 600 °C).

- Seismic measurements confirm strong relations of velocity anisotropy, shear wave splitting and shear wave polarization to the structural grain of the rocks (foliation, lineation).
- Ultrasonic laboratory measurements of COSC-1 samples, from this and previous studies, illustrate that seismic anisotropy is an important parameter that affects our interpretation of Caledonian orogenic processes and crustal dynamics. These results may directly be applied to other orogen settings with ongoing collisions, such as the Himalaya-Tibet orogen, where significant anisotropy is observed in the mid and lower crust.
- Amphibolites and biotite bearing specimens are significantly anisotropic with AVp ranging from 8.9 % to 19.7%, and maximum AVs exceeding 10 %. Felsic gneisses are considerably less anisotropic, with AVp of <7 % and AVs of <6 %.
- Among the eight samples, only one sample (309, felsic gneiss) showed a reduction in P-wave and S-wave anisotropy as a function of increasing temperature, whereas sample 146, Layered felsic gneiss and amphibolite, showed S-wave anisotropy as a function of increasing temperature.
- There is a general correlation between seismic anisotropy and AMS in samples where paramagnetic minerals control the AMS. An observed extra complication is introduced by the presence of ferromagnetic minerals in the felsic gneisses (sample 248) or artificially high degree of anisotropy generated in samples with  $k_{\text{mean}}$  close to zero (felsic gneiss, sample 309).
- To better understand the relationship between seismic anisotropy and AMS, we constructed a flow chart that describes how these two properties relate in terms of mean (bulk) susceptibility and mineral composition. The aim of this chart is to raise awareness and improve the interpretability of AMS data, used as a petrofabric indicator and indirectly as an indicator for seismic anisotropy.

## Acknowledgements

We thank people involved with the Drilling project COSC-1 and the Swedish Scientific Drilling Program (SSDP), for support and access to sample material used in this study. The International Continental Scientific Drilling Program (ICSD) supported the drilling operation. We are grateful for the very constructive and helpful reviews of R. Punturo, K. Michibayashi, Shaocheng Ji and the editor Philippe Agard. These reviews greatly improved the quality of the manuscript. We acknowledge the Swedish Research Council for financial support through the project 2018-03414, awarded to B. Almqvist.

## References:

- Abramson, E. H., J. M. Brown, L. J. Slutsky, and J. Zaug (1997), The elastic constants of San Carlos olivine to 17 GPa, *J. Geophys. Res.*, 102, 12,253–12,263, doi:10.1029/97JB00682.
- Aleksandrov, K. S., and T. V. Ryzhova (1961), Elastic properties of rock forming minerals 2 layered silicates, *Bull. Acad. Sci. USSR Geophys. Sr.*, 11, 871–875.
- Aleksandrov, K. S., U. V. Alchikov, B. P. Belikov, B. I. Zaslavskii, and A. I. Krupnyi (1974), Velocities of elastic waves in minerals at atmospheric pressure and increasing precision of elastic constants by means of EVM [in Russian], *Izv. Acad. Sci. USSR, Geo. Ser.*, 10, 15–24.

- Alkhalifah, T., 1998. Acoustic approximations for processing in transversely isotropic media, *Geophysics*, 63(2), 623–631.
- Alkhalifah, T., 2000. An acoustic wave equation for anisotropic media, *Geophysics*, 65(4), 1239–1250.
- Almqvist, B. S. G., D. Mainprice, C. Madonna, L. Burlini, and A. M. Hirt (2011), Application of differential effective medium, magnetic pore fabric analysis, and X-ray microtomography to calculate elastic properties of porous and anisotropic rock aggregates, *J. Geophys. Res.*, 116.
- Almqvist, B. S. G., A. M. Hirt, M. Herwegh, A. Ebert, J. M. Walter, B. Leiss, and L. Burlini (2013), Seismic anisotropy in the Morcles nappe shear zone: Implication for seismic imaging of crustal scale shear zones, *Tectonophysics*, 603, 162–178.
- Almqvist, B. S. G., and Mainprice, D., 2017. Seismic properties and anisotropy of the continental crust: Predictions based on mineral texture and rock microstructure, *Rev. Geophys.*, 55, 367–433, doi:10.1002/2016RG000552.
- Almqvist, B.S.G., Misra, S., Klonowska, I., Mainprice, D., Majka, I. (2015), Ultrasonic velocity drops and anisotropy in mica-schist analogues due to melting with implications for seismic imaging of continental crust, *Earth and Planetary Science Letters*, 425, 21–33.
- Almqvist, B. S. G. Cyprych, D. Piazzolo, S. (2021), Seismic anisotropy of mid crustal orogenic nappes and their bounding structures: An example from the Middle Allochthon (Seve Nappe) of the Central Scandinavian Caledonides, *Tectonophysics*, 229045, <https://doi.org/10.1016/j.tecto.2021.229045>
- Anderson, D. L., B. Minster, and D. Cole (1977), The effect of oriented cracks on seismic velocities, *J. Geophys. Res.*, 79, 4011–4015, doi:10.1029/JB079i026p04011.
- Andersen, T., 1998. Extensional tectonics in the Caledonides of southern Norway, an overview, *Tectonophysics*, 285, 333–351.
- Audet, P. (2015), Layered crustal anisotropy around the San Andreas Fault near Parkfield, California, *J. Geophys. Res. Solid Earth*, 120, 3527–3543, doi:10.1002/2014JB011821.
- Babuska, V., and M. Cara (1991), *Seismic Anisotropy in the Earth*, pp. 217, Kluwer Acad., Netherlands. Babuska, V., J. Fiala, M. Kumazawa, I. Ohno, and Y. Sumino (1978), Elastic properties of garnet solid-solutions series, *Phys. Earth Planet. Int.*, 16, 157–176.
- Backus, G. E. (1962), Long wave elastic anisotropy produced by horizontal layering, *J. Geophys. Res.*, 67, 4427–4440, doi:10.1029/JZ067i011p04427.
- Barruol, G., and D. Mainprice (1993), 3-D seismic velocities calculated from lattice-preferred orientation and reflectivity of a lower crustal section: Examples of the Val Sesia section (Ivrea zone, northern Italy), *Geophys. J. Int.*, 115, 1169–1188.
- Barruol, G., and H. Kern (1996), Seismic anisotropy and shear-wave splitting in lower-crustal and upper-mantle rocks from the Ivrea Zone— Experimental and calculated data, *Phys. Earth Planet. Inter.*, 95, 175–194.
- Bazargan, M. Vachon, R. Hieronymus, Ch. F. (2019), Evolution of the statistical distribution of crystal orientations in time- and space-varying viscous flows, *Geophysical Journal International*, 218, Issue 2, Pages 773–786, <https://doi.org/10.1093/gji/ggz174>

Bergman, S., Stephens, M.B., Andersson, J., Kathol, B., and Bergman, T., 2012, Bedrock map of Sweden, scale 1: 1 million: Sveriges geologiska undersökning K, v. 423.

Biedermann, A.R. (2018), Magnetic anisotropy in single crystals: a review, *Geosciences*, 8, 302, doi:10.3390/geosciences8080302.

Biedermann, A.R., Bender Koch, C., Pettke, T., Hirt, A.M. (2015), Magnetic anisotropy in natural amphibole crystals, *American Mineralogist*, 100, 1940-1951.

Biedermann, A.R., Kunze, K., Zappone, A.S. (2020), Crystallographic preferred orientation, magnetic and seismic anisotropy in rocks from the Finero peridotite, Ivrea-Verbano Zone, Northern Italy – interplay of anisotropy contributions from different minerals, *Tectonophysics*, 782-783, doi:10.1016/j.tecto.2020.228424.

Birch, F. (1960), The velocity of compressional waves in rocks to 10 kilobars: 1., *Journal of Geophysical Research*, 65, 1083-1102.

Birch, F. (1961), The velocity of compressional waves in rock to 10 kilobars: 2., *Journal of Geophysical Research*, 66, 2199-2224.

Borradaile, G. J. Henry, B. (1997), Tectonic applications of magnetic susceptibility and its anisotropy, *Earth-Sci. Rev.*, 42, pp. 47-93

Borradaile, G. J., & Jackson, M. J. (2004). Anisotropy of magnetic susceptibility (AMS): Magnetic petrofabrics of deformed rocks. *Geological Society Special Publication*, 238, 299-360. <https://doi.org/10.1144/GSL.SP.2004.238.01.18>

Borradaile, G.J., Jackson, M. (2010), Structural geology, petrofabrics and magnetic fabrics (AMS, AARM, AIRM), *Journal of Structural Geology*, 32, 1519-1551.

Brown, J. M., R. J. Angel, and N. L. Ross (2016), Elasticity of plagioclase feldspars, *J. Geophys. Res. Solid Earth*, 121, 663–675, doi:10.1002/2015JB012736.

Brown, J. M., and E. H. Abramson (2016), Elasticity of calcium and calcium-sodium amphiboles, *Phys. Earth Planet. Inter.*, 261, 161–171.

Burke, M.M., Fountain, D.M. (1990), Seismic properties of rocks exposure of extended continental crust – new laboratory measurements from the Ivrea Zone, *Tectonophysics*, 182, 119-146.

Burlini, L., Fountain, D.M. (1993), Seismic anisotropy of metapelites from the Ivrea-Verbano zone and Serie dei Laghi (N. Italy), *Physics of the Earth and Planetary Interiors*, 78, 301-317.

Carpenter, M. A., E. K. H. Salje, A. Graeme-Barber, B. Wrucki, M. T. Dove, and K. S. Knight (1998), Calibration of excess thermodynamic properties and elastic constant variations associated with the alpha-beta phase transition in quartz, *Am. Mineral.*, 83, 2–22.

Chai, M., J. M. Brown, and L. J. Slutsky (1997), The elastic constants of an aluminous orthopyroxene to 12.5 GPa, *J. Geophys. Res.*, 102, 14,779–14,785, doi:10.1029/97JB00893.

Chen, C.-C., C.-C. Lin, L.-G. Liu, V. Sinogeikin, and J. D. Bass (2001), Elasticity of single-crystal calcite and rhodochrosite by Brillouin spectroscopy, *Am. Mineral.*, 86, 1525–1529.

- Cholach, P.Y., Schmitt, D.R. 2006. Intrinsic elasticity of a textured transversely isotropic muscovite aggregate: Comparisons to the seismic anisotropy of schists and shales. *J. Geophys. Res.* 111, B09410, doi:10.1029/2005JB004158.
- Christensen, N. I. (1965), Compressional wave velocities in metamorphic rocks at pressure to 10 kilobars, *J. Geophys. Res.*, 70, 6147–6164, doi:10.1029/JZ070i024p06147.
- Christensen, N. I. (1971), Shear wave propagation in rocks, *Nature*, 229, 549–550.
- Christensen, N. I. (1974), Compressional wave velocities in possible mantle rocks to pressures of 30 kilobars, *J. Geophys. Res.*, 79, 407–412, doi:10.1029/JB079i002p00407.
- Christensen, N. I. (1979), Compressional wave velocities in rocks at high temperatures and pressures, critical thermal gradients, and crustal low-velocity zones, *J. Geophys. Res.*, 84, 6849–6857, doi:10.1029/JB084iB12p06849.
- Christensen, N. I., and W. D. Mooney (1995), Seismic velocity structure and composition of the continental crust: A global view, *J. Geophys. Res.*, 100, 9761–9788, doi:10.1029/95JB00259.
- Christensen, N. I. (1996), Poisson's ratio and crustal seismology, *J. Geophys. Res.*, 101, 3139–3156, doi:10.1029/95JB03446.
- Cyprych, D. Piazzolo, S. Bjarne S.G. Almqvist, (2017), "Seismic anisotropy from compositional banding in granulites from the deep magmatic arc of Fiordland New Zealand", *Earth and Planetary Science Letters*
- Eberhart-Phillips, D., Han, D., Zoback, M. (1989), Empirical relationships among seismic velocity, effective pressure, porosity, and clay content in sandstone, *Geophysics*, 54, 82-89.
- Ellwood, B. B., and Whitney, J. A. (1980), Magnetic fabric of the Elberton Granite, northeast Georgia, *J. Geophys. Res.*, 85( B3), 1481– 1486, doi:10.1029/JB085iB03p01481.
- Elger, J., Berndt, C., Kästner, F., Pierdominici, S., Kück, J., Almqvist, B.S.G., Juhlin, C., Lorenz, H. (2021), Core-log-seismic integration in metamorphic rocks and its implication for the regional geology: A case study for the ICDP drilling project COSC-1, Sweden, *Geochemistry, Geophysics, Geosystems*, doi:10.1029/2020GC009276.
- Emmermann, R. Lauterjung, J. (1997), The German Continental Deep Drilling Program KTB: Overview and major results, *J. Geophys. Res.*, Volume102, Pages 18179-18201.
- Feinberg, J.M., Wenk, H.-R., Scott, G.R., Renne, P.R. (2006), Preferred orientation and anisotropy of seismic and magnetic properties in gabbro-norites from the Bushveld layered intrusion, *Tectonophysics* 420, 345-356.
- Ferri, F., Burlini, L., Sassi, R. (2007), Seismic properties of lower crustal xenoliths from El Hoyazo (SE Spain): Experimental evidence up to partial melting, *Earth and Planetary Science Letters*, 253, 239-253.
- Ferri, F., Burlini, L., Cesare, B. (2016), Effect of partial melting on Vp and Vs in crustal enclaves from Mazarrón (SE Spain), *Tectonophysics*, 671, 139-150.



- Fountain, D. (1976), The Ivrea-Verbano and Strona-Ceneri Zones, northern Italy: a cross-section of the continental crust – new evidence from seismic velocities of rock samples, *Tectonophysics*, 33, 145-165.
- Gee, D., (1975). A tectonic model for central part of Scandinavian Caledonides, *Am. J. Sci.*, 275-A, 468–515.
- Gee, D., (1978). Nappe displacement in Scandinavian Caledonides, *Tectonophysics*, 47(3-4), 393–419.
- Gee, D. & Sturt, B., (eds) (1985), *The Caledonide Orogen - Scandinavia and Related Areas*, John Wiley & Sons Ltd.
- Gee, D., Fossen, H., Henriksen, N. & Higgins, A., 2008. From the early Paleozoic platforms of Baltica and Laurentia to the Caledonide orogen of Scandinavia and Greenland, *Episodes*, 31(1), 44–51.
- Gee, D., Juhlin, C., Pascal, C. & Robinson, P., 2010. Collisional Orogeny in the Scandinavian Caledonides (COSC), *GFF*, 132(1), 29–44.
- Gee, D. G., Janák, M., Majka, J., Robinson, P., and van Roermund, H. Subduction along and within the baltoscandian margin during closing of the lapetus ocean and Baltica-laurentia collision, *Lithosphere*, 5, 169–178, <https://doi.org/10.1130/L220.1>, 2013.
- Giuntoli F., Menegon L., Warren C. (2018) Replacement reactions and deformation by dissolution and precipitation processes in amphibolites. *Journal of Metamorphic Geology*, 36, 1263–1286, <https://doi.org/10.1111/jmg.12445>
- Giuntoli F., Menegon L., Warren C. J., Darling J., Anderson M. W. (2020). Protracted shearing at midcrustal conditions during large-scale thrusting in the Scandinavian Caledonides. *Tectonics*, 39, e2020TC006267, <https://doi.org/10.1019/2020TC006267>
- Graham, J. W. (1966), Significance of magnetic anisotropy in Appalachian sedimentary rocks. In: *The Earth Beneath the Continents* (eds. Steinhardt, J. S., Smith, T. J.), Geophysical Monograph American Geophysical Union, 10, 627-648.
- Hacker, B. R., P. B. Kellman, and M. D. Behn (2015), Continental lower crust, *Annu. Rev. Earth Planet. Sci.*, 43, 157–205.
- Hedin, P., Juhlin, C. & Gee, D., (2012). Seismic imaging of the Scandinavian Caledonides to define ICDP drilling sites, *Tectonophysics*, 554-557, 30–41.
- Hedin, P., Malehmir, A., Gee, D.G., Juhlin, C., Dyrelus, D. (2014), 3D interpretation by integrating seismic and potential field data in the vicinity of the proposed COSC-1 drill site, central Swedish Caledonides, Geological Society, London, Special Publications, 390, 301-319.
- Hedin, P., Almqvist, B. S. G., Berthet, T., Juhlin, C., Buske, S., Simon, H., Giese, R., Krauß, F., Rosberg, J. E., Alm, P. G., (2016). 3D reflection seismic imaging at the 2.5 km deep COSC-1 scientific borehole, central Scandinavian Caledonides, *Tectonophysics*, 689, 40–55.
- Henry, B. (1983), interpretation QUANTITATIVE DE L'ANISOTROPIE DE susceptibilit  magn tque, *Tectonophysics*, 91 (1983) 165-177

- Hirn, A., Damotte, B., Torreilles, G., ECORS Scientific Party (1987), Crustal reflection seismics: the contributions of oblique, low frequency and shear wave illuminations, *Geophysical Journal International*, 89, 287-296.
- Holmberg, J. (2017), Pressure-Temperature-time Constraints on the Deep Subduction and Emplacement of the Seve Nappe Complex in Jämtland and Southern Västerbotten, Scandinavian Caledonides, *Examensarbete vid Institutionen för geovetenskaper*, ISSN 1650-6553 Nr 418
- Hrouda, F. Janák, L. Rejl, J. Weiss, (1971), The use of magnetic susceptibility anisotropy for estimating the ferromagnetic mineral fabrics of metamorphic rocks, *Geol. Rundsch.*, 60, pp. 1124-1142.
- Hrouda, F. (1986), The effect of quartz on the magnetic anisotropy of quartzite, *Studia Geoph. et Geod.*, 30, 39-45.
- Hrouda, F. (2004), Problems in interpreting AMS parameters in diamagnetic rocks, *Geological Society of London, Special Publications*, 238, 49-59.
- Isaak, D. G., I. Ohno, and P. C. Lee (2006), The elastic constants of monoclinic single-crystal chrome-diopside to 1300 K, *Phys. Chem. Miner.*, 32, 691–699.
- Ji, S. and M. Salisbury, 1993, Shear-wave velocities, anisotropy and splitting in the high grade mylonites, *Tectonophysics*, 221, 3/4, 453-473.
- Ji, S., M. Salisbury, and S. Hanmer (1993), Petrofabrics, P-wave anisotropy and seismic reflectivity of high-grade tectonites, *Tectonophysics*, 222, 199-225.
- Ji, S., S. Rondenay, M. Mareschal & G. Senechal, 1996. Obliquity between seismic and electrical anisotropies as an indicator of movement sense for ductile mantle shear zones. *Geology*, 24, 1033-1036
- Ji et al., 1997. Seismic reflectivity of a finely layered, granulite-facies ductile shear zone in the southern Grenville Province (Quebec), *Tectonophysics*, 279 (1-4), 113-133.
- Ji, S., Wang, Q., Xia, B., 2002. *Handbook of Seismic Properties of Minerals, Rocks and Ores*. Polytechnic International Press, 630 pp, Montreal (Canada).
- Ji, S., K. Saruwatari, D. Mainprice, R. Wirth, Z. Xu, and B. Xia (2003), Microstructure, petrofabrics and seismic properties of ultra high-pressure eclogites from Sulu region, China: Implications for rheology of subducted continental crust and origin of mantle reflections, *Tectonophysics*, 370, 49–76.
- Ji, S., Q. Wang, D. Marcotte, M. H. Salisbury, and Z. Xu (2007), P wave velocities, anisotropy and hysteresis in ultrahigh-pressure metamorphic rocks as a function of confining pressure, *J. Geophys. Res.*, 112, B09204, doi:10.1029/2006JB004867.
- Ji, S., T. Shao, K. Michibayashi, C. Long, Q. Wang, Y. Kondo, W. Zhao, H. Wang, and M. H. Salisbury (2013), A new calibration of seismic velocities, anisotropy, fabrics, and elastic moduli of amphibole-rich rocks, *J. Geophys. Res. Solid Earth*, 118, 4699–4728, doi:10.1002/jgrb.50352.
- Ji, S., T. Shao, M. H. Salisbury, S. Sun, K. Michibayashi, W. Zhao, C. Long, F. Liang, and T. Satsukawa (2014), Plagioclase preferred orientation and induced seismic anisotropy in mafic igneous rocks, *J. Geophys. Res. Solid Earth*, 119, 8064–8088, doi:10.1002/2014JB011352.

Ji, S., T. Shao, K. Michibayashi, S. Oya, T. Satsukawa, Q. Wang, W. Zhao, and M. Salisbury (2015), Magnitude and symmetry of seismic anisotropy in mica- and amphibole-bearing metamorphic rocks and implications for tectonic interpretation of seismic data from the southeast Tibetan Plateau, *J. Geophys. Res. Solid Earth*, 120, 629–631.

Juhlin, C., Hedin, P., Gee, D., Lorenz, H., Kalscheuer, T. & Yan, P., 2016. Seismic imaging in the eastern Scandinavian Caledonides: siting the 2.5 km deep COSC-2 borehole, central Sweden, *Solid Earth*, 7, 769–787.

Kästner, F., Pierdominici, S., Elger, J., Zappone, A., Kuck, J. & Berndt, C., 2020. Correlation of core and downhole seismic velocities in high-pressure metamorphic rocks: a case study for the COSC-1 borehole, Sweden, *Solid Earth*, 11, 607–626., <https://doi.org/10.5194/se-11-607-2020>

Kern, H. (1978), The effect of high temperature and high confining pressure on compressional wave velocities in quartz-bearing and quartz-free igneous and metamorphic rocks, *Tectonophysics*, 44, 185–203.

Kern, H. (1979), Effect of high-low quartz transition on compressional and shear wave velocities in rocks under high pressure, *Phys. Chem. Miner.*, 4, 161–171.

Kern, H., and A. Richter (1981), Temperature derivatives of compressional and shear wave velocities in crustal and mantle rocks at 6 kbar confining pressure, *J. Geophys.*, 49, 47–56.

Kern, H.: Elastic-wave velocity in crustal and mantle rocks at high pressure and temperature: the role of the high-low quartz transition and of dehydration reactions, *Phys. Earth Planet. In.*, 29, 12–23, [https://doi.org/10.1016/0031-9201\(82\)90133-5](https://doi.org/10.1016/0031-9201(82)90133-5), 1982.

Kern, H.: Laboratory seismic measurements: an aid in the interpretation of seismic field data, *Terra Nova*, 2, 617–628, <https://doi.org/10.1111/j.1365-3121.1990.tb00127.x>, 1990.

Kern, H. and Wenk, H.-R.: Fabric-related velocity anisotropy and shear wave splitting in rocks from the Santa Rosa Mylonite Zone, California, *J. Geophys. Res.*, 95, 11213–11223, <https://doi.org/10.1029/JB095iB07p11213>, 1990.

Kern H., Schmidt R., and Popp T.: The velocity and density structure of the 4000m crustal segment at the KTB drilling site and their relationship to lithological and microstructural characteristics of the rocks: an experimental approach, *Scientific Drilling*, 2, 130–145, 1991.

Kern, H., L. Burlini, and I. V. Ashchepkov (1995), Fabric-related seismic anisotropy in upper-mantle xenoliths: Evidence from measurements and calculations, *Phys. Earth Planet. Inter.*, 95, 195–209.

Kern, H., S. Gao, and Q.-S. Liu (1996), Seismic properties and densities of middle and lower crustal rocks exposed along the North China Geoscience Transect, *Earth Planet. Sci. Lett.*, 139, 439–455.

Kern, H., Liu, B., Popp, T., (1997) Relationship between anisotropy of P and S wave velocities and anisotropy of attenuation in serpentinite and amphibolite, *journal of geophysical research*, vol. 102, no. b2, pages 3051-306

Kern, H., S. Gao, Z. Jin, T. Popp, and S. Jin (1999), Petrophysical studies on rocks from the Dabie ultrahigh-pressure (UHP) metamorphic belt, Central China: Implications for the composition and delamination of the lower crust, *Tectonophysics*, 301, 191–215.

Kern, H., Z. Jin, S. Gao, T. Popp, and Z. Xu (2002), Physical properties of ultrahigh-pressure metamorphic rocks from the Sulu terrain, eastern central China: Implications for the seismic structure at the Donghai (CCSD) drilling site, *Tectonophysics*, 354, 315–330.

Kern, H., T. I. Ivankina, A. N. Nikitin, T. Lokajíček, and Z. Pros (2008), The effect of oriented microcracks and crystallographic and shape preferred orientation on bulk elastic anisotropy of a foliated biotite gneiss from Outokumpu, *Tectonophysics*, 457, 143–149.

Khan, A. M. (1962), The Anisotropy of Magnetic Susceptibility of Some Igneous and Metamorphic Rocks, *Journal OF geophysical SRCH* volume 67, No. 7

Knight, M. D. AND WALKER, G. P. L. (1988), Magma Flow Directions in Dikes of the Koolau Complex Determined From Magnetic Fabric Studies, *JOURNAL OF GEOPHYSICAL RESEARCH*, VOL. 93, NO. B5, PAGES 4301-4319,

Ko, B., and H. Jung (2015), Crystal preferred orientation of an amphibole experimentally deformed by simple shear, *Nat. Commun.*, 6, doi:10.1038/ncomms7586.

Lagroix, F., Borradaile, G.J. (2000), Magnetic fabric interpretation complicated by inclusions in mafic silicates, *Tectonophysics*, 325, 207-225.

Lloyd, G. E., and J.-M. Kendall (2005), Petrofabric-derived seismic properties of a mylonitic quartz simple shear zone: Implications for seismic reflection profiling, *Geol. Soc. London, Spec. Publ.*, 240, 75–94.

Lloyd, G. E., R. W. H. Butler, M. Casey, and D. Mainprice (2009), Mica, deformation fabrics and the seismic properties of the continental crust, *Earth Planet. Sci. Lett.*, 288, 320–328.

Lloyd, G. E., R. W. H. Butler, M. Casey, D. L. Ratham, and D. Mainprice (2011b), Constraints on the seismic properties of the middle and lower continental crust, *Geol. Soc. London, Spec. Publ.*, 360, 7–32.

Lloyd, G. E., J. M. Halliday, R. W. H. Butler, M. Casey, J.-M. Kendall, J. Wookey, and D. Mainprice (2011b), From crystal to crustal: Petrofabric- derived seismic modelling of regional tectonics, *Geol. Soc. London, Spec. Publ.*, 360, 19–78.

Lorenz, H. Rosberg, J. E. Juhlin, Ch. Bjelm, L. Almqvist, B. G. Berthet, T. Conze, R. Gee, D. G. Klonowska, I. Pascal, Ch. Pedersen, K. Roberts, N. Tsang, Ch. (2015), COSC-1 operational report - Operational data sets. GFZ Data Services. <https://doi.org/10.1594/GFZ.SDDB.ICDP.5054.2015>

Lorenz, H. Juhlin, Ch. Rosberg, J. E. Bazargan, M. Klonowska, I. Kück, J. Lescloutre, R. Rejkjær, S. Westmeijer, G. Ziemniak, G. (2021), COSC-2 operational report - Operational data sets. GFZ Data Services. <https://doi.org/10.5880/ICDP.5054.003>

Madonna, C., Almqvist, B.S.G., Saenger, E.H. (2012), Digital rock physics: numerical prediction of pressure-dependent ultrasonic velocities using micro-CT imaging, *Geophysical Journal International*, 189, 1475-1482.

Mainprice, D. Nicolas, A. (1989), Development of shape and lattice preferred orientations: application to the seismic anisotropy of the lower crust, *Journal of Structural Geology*, Volume 11, Issues 1–2, Pages 175-189,

Mainprice, D. 1990, A FORTRAN program to calculate seismic anisotropy from the lattice preferred orientation of minerals, *Computers & Geosciences*, Volume 16, Issue 3, Pages 385-393,

Mainprice, D. (2000), The estimation of seismic properties of rocks with heterogeneous microstructures using a local cluster model— Preliminary results, *Phys. Chem. Earth*, 25, 155–161.

Mainprice, D. (2007), Seismic anisotropy of the deep Earth from a mineral and rock physics perspective, in *Treatise in Geophysics*, vol. 2, edited by G. Schubert, pp. 437–492, Elsevier, Oxford.

Mainprice, D. (2015), Seismic anisotropy of the deep Earth from a mineral and rock physics perspective, in *Treatise in Geophysics*, 2nd ed., vol. 2, edited by G. Schubert, pp. 487–539, Elsevier, Oxford.

Mainprice, D., G. Barruol, and W. Ben Ismaïl (2000), The seismic anisotropy of the Earth's mantle: From single crystal to polycrystal, in *Earth's Deep Interior: Mineral Physics and Tomography From the Atomic to the Global Scale*, *Geophys. Monogr. Ser.*, vol. 117, pp. 237–264, AGU, Washington, D. C.

Mamtani, M., Piaolo, S., Greiling, R.O., Kontny, A., Hrouda, F. 2011. Process of magnetite fabric development during granite deformation. *Earth Planet. Sci. Lett.* 308, 77-89.

Martín-Hernandez, F., Hirt, A.M. (2003), The anisotropy of magnetic susceptibility in biotite, muscovite and chlorite single crystals, *Tectonophysics*, 367, 13–28.

Merz, L. Almqvist, B. G. S., Grimmer, J.C., Kontny, A. 2010. Magnetic fabric development in the Lower Seve thrust from the COSC-1 drilling, Swedish Caledonides, *Tectonophysics*, Volume 751, Pages 212-228.

Mooney, W. D., and R. Meissner (1992), Multi-genetic origin of crustal reflectivity: A review of seismic reflection profiling of the continental lower crust and Moho, in *Continental Lower Crust*, vol. 23, edited by D. M. Fountain, R. Arculus, and R. W. Kay, pp. 45–79, Elsevier, Amsterdam.

Mooney, W. D. (2015), Crust and lithospheric structure—Global crustal structure, in *Treatise of Geophysics*, 2nd ed., vol. 1, pp. 329–390, Elsevier, Amsterdam.

Motra, H. B. and Stutz, H. H. Geomechanical Rock Properties Using Pressure and Temperature Dependence of Elastic P and S-Wave Velocities, *Geotechnical and Geological Engineering*, 36, 3751–3766.

Ohno, I., K. Harada, and C. Yoshitomi (2006), Temperature variation of elastic constants of quartz across the  $\alpha$ - $\beta$  transition, *Phys. Chem. Miner.*, 33, 1–9.

Owens, W.H. Rutter, E.H. (1978), The development of magnetic susceptibility anisotropy through crystallographic preferred orientation in a calcite rock, *Physics of the Earth and Planetary Interiors*, Volume 16, Issue 3, Pages 215-222,

Paaschier, C. W., and R. Trouw (2005), *Microtectonics*, pp. 366, Springer, Heidelberg, Berlin.

Piaolo, S., & Passchier, C. W. (2002). Controls on lineation development in low to medium grade shear zones: a study from the Cap de Creus peninsula, NE Spain. *Journal of Structural Geology*, 24(1), 25-44.

Punturo, R. Mamtani, A. M. Fazio, E. Occhipinti, R. (2017), Seismic and magnetic susceptibility anisotropy of middle-lower continental crust: Insights for their potential relationship from a study of



intrusive rocks from the Serre Massif (Calabria, southern Italy), *Tectonophysics* 712–713 (2017) 542–556

Rochette, P., Jackson, M., Aubourg, C. (1992), Rock magnetism and the interpretation of anisotropy of magnetic susceptibility. *Reviews of Geophysics*, 30, 209-226.

Schulte-Pelkum, V. Monsalve, G. Sheehan, A. Pandey. M. R. Sapkota, S. Bilham, R. Wu, F., 2005, Imaging the Indian subcontinent beneath the Himalaya, *Nature*, Vol 435. 1222–1225

Schijns, H. Schmitt, D. R. Heikkinen, P. J. Kukkonen, I. T. (2012), Seismic anisotropy in the crystalline upper crust: observations and modelling from the Outokumpu scientific borehole, Finland, *Geophysical Journal International*, Volume 189, Issue 1, April 2012, Pages 541–553, <https://doi.org/10.1111/j.1365-246X.2012.05358.x>

Shapiro, N. M., Ritzwoller, M. H. Molnar, P. Levin, V., 2004, Thinking and Flow of Tibetan Crust Constrained by Seismic Anisotropy, *science*, Vol. 305, Issue 5681, pp. 233-236

Siegesmund, S., Mosch, S., Scheffzik, Ch., Nikolayev, D.I. (2008). The bowing potential of granitic rocks: rock fabrics, thermal properties and residual strain. *Environmental Geology* 55, 1437-1448.

Simon, H., Buske, S., Krauß, F., Giese, R., Hedin, P. & Juhlin, C., 2017. The derivation of an anisotropic velocity model from a combined surface and borehole seismic survey in crystalline environment at the COSC-1 borehole, central Sweden, *Geophys. J. Int.*, 210(3), 1332–1346.

Simon, H., Buske, S., Hedin, P., Juhlin, C., Krauß, F. & Giese, R., 2019. Anisotropic Kirchhoff pre-stack depth migration at the COSC-1 borehole, central Sweden, *Geophys. J. Int.*, **219**, 66–79

Sun et al., 2012. P-wave velocity differences between surface-derived and core samples from the Sulu ultrahigh-pressure terrane: Implications for in situ velocities at great depths. *Geology*, 40, 651-654

Tatham, D. J., G. E. Lloyd, R. W. H. Butler, and M. Casey (2008), Amphibole and lower crustal seismic properties, *Earth Planet. Sci. Lett.*, 267, 118–128.

Thomsen, L., 1986. Weak elastic anisotropy, *Geophysics*, 51(10), 1954–1966.

Todd, T., Simmons, G. (1972), Effect of pore pressure on the velocity of compressional wave in low-porosity rocks, *Journal of Geophysical Research*, 77, 3731-3743.

Tribaudino, M., Artoni, A., Mavris, Ch., Bersani, D., Lottici, P. P., Belletti, D., (2008), Single-crystal X-ray and Raman investigation on melanophlogite from Varano Marchesi (Parma, Italy). *American Mineralogist* ; 93 (1): 88–94

Ullemeyer, K., D. I. Niklayev, N. I. Christensen, and J. H. Behrmann (2011), Evaluation of intrinsic velocity-pressure trends from low-pressure P-wave velocity measurements in rocks containing microcracks, *Geophys. J. Int.*, 185, 1312–1320.

Vachon, R. Bazargan, M. Hieronymus, Ch. F. Ronchin, E. Almqvist, B. G. (2021), Crystal rotations and alignment in spatially varying magma flows: 2-D examples of common subvolcanic flow geometries, *Geophysical Journal International*, Volume 226, Issue 1, Pages 709–727, <https://doi.org/10.1093/gji/ggab127>

- Valcke, S. L. A., M. Casey, G. E. Lloyd, J.-M. Kendall, and Q. J. Fisher (2006), Lattice preferred orientation and seismic anisotropy in sedimentary rocks, *Geophys. J. Int.*, 166, 652–666.
- Vaughan, M. T., and S. Guggenheim (1986), Elasticity of muscovite and its relationship to crystal structure, *J. Geophys. Res.*, 91, 4657–4664, doi:10.1029/JB091iB05p04657.
- Waeselmann, N., J. M. Brown, R. J. Angel, N. Ross, J. Zhao, and W. Kaminsky (2016), The elastic tensor of monoclinic alkali feldspars, *Am. Mineral.*, 101, 1228–1231.
- Walsh, J. B. (1965), The effect of cracks on the compressibility of rock, *J. Geophys. Res.*, 70, 381–389, doi:10.1029/JZ070i002p00381.
- Wenk, H.-R., R. N. Vasin, H. Kern, S. Matthies, S. C. Vogel, and T. I. Ivankina (2012), Revisiting elastic anisotropy of biotite gneiss from the Outokumpu scientific drill hole based on new texture measurements and texture-based velocity calculations, *Tectonophysics*, 570–571, 123–134.
- Wenning, Q., B. S. G. Almqvist, P. Hedin, and A. Zappone (2016), Seismic anisotropy in mid to lower orogenic crust: Insights from laboratory measurements of  $V_p$  and  $V_s$  in drill core from central Scandinavian Caledonides, *Tectonophysics*, doi:10.1016/j.tecto.2016.07.002.
- Whitney, D. L. Evans, B. W. (2010), Abbreviations for names of rock-forming minerals, *American Mineralogist*, Volume 95, pages 185–187.
- Wyllie, M. R. J., A. R. Gregory, and G. H. F. Gardner (1968), An experimental investigation of factors affecting elastic wave velocities in porous media, *Geophysics*, 23, 459–493.
- Zappone, A., and P. M. Benson (2013), Effect of phase transitions on seismic properties of metapelites: A new high-temperature laboratory calibration, *Geology*, 41, 463–466.

Credit Author Statement

Mohsen Bazargan (MB), Bjarne Almqvist (BA), Sandra Piazzolo (SP), Hem Motra (HM) and Christoph Hieronymus (CH) designed and developed the concept for the study together. Samples were collected by MB and BA. Laboratory ultrasonic and magnetic measurements were made by MB, HM and BA at Christian Albert University of Kiel and Uppsala University. MB, BA and SP prepared the first draft of the manuscript. All authors contributed to the editing of the manuscript.

### Declaration of interests

☒ The authors declare that they have no known competing financial interests or personal relationships that could have appeared to influence the work reported in this paper.

☐ The authors declare the following financial interests/personal relationships which may be considered as potential competing interests:

Table 1. Modal mineral composition (%) of samples in the study

Lithological group	Rock type	Sample no.	Qz	Pl	Kfs	Cal	Amph (hbl)	Cpx (Di)	Bi	Mu	Other (Ep, Ap, opq)
felsic gneiss	qtz-cal gneiss	248	50	<5	≤5	35				≤5	
	qtz-feldspar gneiss	302	50	3	1						
	qtz-feldspar gneiss	302	2			10-		10			
	qtz-feldspar gneiss	302	5	50-60		15					
intermediate gneiss	Bt gneiss	316	30	2					2		
mafic gneiss	Bt bearing amphibolite	340		5			60		5		
	amphibolite	274		2					3-		
	amphibolite	193		5	5		60		5		5
	amphibolite	193		3							
layered felsic-mafic gneiss	qtz feldspatic gneiss layer	146	60	2	1	3-5		≤2			

Mineral abbreviations from Whitney and Evans (2010): Qz - quartz; Pl - plagioclase; Kfs - potassium feldspar; hbl - hornblende; Di - diopside; Bi - biotite; Mu - muscovite; Ep - epidote; Ap - apatite; opq - opaque

Table 2: Compilation ultrasonic wave speed measurements at 600 MPa. Vp is reported with respect to X, Y and Z axes, and Vs with respect to the polarization direction. The right-most columns show the linear strain (%) of the samples, comparing room conditions with pressure of 600 MPa.

[illegible]



146	2.787	6.	6.	5.	6.		3.	3.	3.	3.	3.	3.	3.	10.	0.	0.	0.
		4	2	9	2	8.8	8	7	7	5	4	5	6	66	4	4	7
		8	6	2	2	70	2	7	4	8	3	2	4	3	3	9	4
		0	3	8	4		0	8	7	2	1	0	6	3	0	2	3

Table 3: Compilation of data from ultrasonic laboratory experiments at 600 °C and 600 MPa. Vp is reported with respect to X, Y and Z axes, and Vs with respect to the polarization direction. The right-most three columns show the linear strain (%) of the samples, comparing room conditions with pressure and temperature of 600 MPa and 600 °C.

Sample Name	Density y (g/cm <sup>3</sup> )	Vp (km/s)				A- Vp (%)	Vs (km/s)								A- Vs (%)	ε		
		m					m											
		x	y	z	ea n		yx	zx	xy	zy	yz	xz	ea n	x		y	z	
felsic gneiss																		
248	2.714	6.	6.	5.	6.		3.	3.	3.	3.	3.	3.		0.	0.	1.		
		2	0	9	0	5.8	3	2	3	2	4	3	3	6.6	9	9	1	
		6	9	0	8	35	4	3	7	6	8	4	5	51	4	2	8	
		2	5	7	8		1	4	1	2	5	9	7		9	8	0	
309	2.602	6.	6.	5.	5.		3.	3.	3.	3.	3.	3.		0.	0.	0.		
		0	0	7	9	4.6	5	5	5	5	7	6	6	6.1	3	4	6	
		4	7	9	7	61	8	5	5	5	7	6	1	48	7	6	1	
		2	7	9	3		3	0	3	6	2	2	3		6	4	1	
362	2.795	6.	6.	6.	6.		3.	3.	3.	3.	3.	3.		0.	0.	0.		
		4	3	0	5	6.4	4	4	5	4	6	5	5	6.1	3	4	6	
		9	2	3	0	72	7	6	5	1	3	1	1	60	5	5	2	
		0	7	2	0		3	8	9	9	5	3	1		6	7	4	
Bt gneiss																		
316	2.964	7.	6.	5.	6.		2.	2.	3.	2.	4.	4.	3.	37.	0.	0.	1.	
		2	4	5	3	23.	8	8	7	9	0	1	4	86	4	7	2	
		0	5	0	2	805	8	5	8	7	2	5	4	9	1	4	0	
		8	2	3	1		0	0	2	3	1	4	3		1	7	4	
mafic gneiss																		
193	2.992	7.	6.	6.	6.		4.	3.	4.	3.	3.	3.		0.	0.	0.		
		3	9	4	9	13.	2	9	0	7	8	8	9	11.	1	2	4	
		5	3	2	0	545	5	1	8	9	2	7	5	57	7	9	7	
		7	9	2	6		5	2	5	7	5	3	8	7	7	3	7	
274	2.988	7.	6.	6.	6.		3.	3.	3.	3.	4.	3.	3.		0.	0.	0.	
		2	9	5	8	10.	7	8	8	7	1	8	8	9.9	1	3	5	
		1	4	2	9	034	9	0	3	3	1	7	5	01	9	5	0	
		3	0	1	1		0	9	4	0	2	1	8		4	1	7	
340	2.980	7.	7.	6.	6.		3.	3.	4.	3.	4.	3.	3.	22.	0.	0.	0.	
		5	0	1	9	20.	5	5	1	4	3	5	7	56	1	2	6	
		3	7	1	0	546	3	2	0	7	2	9	6	8	9	6	7	
		5	3	6	8		1	7	9	2	0	8	0		9	5	3	

Layered  
Felsic-Mafic  
Gneiss

146

2.735

6.	6.	5.	6.		3.	3.	3.	3.	3.	3.	3.		0.	0.	0.
3	0	7	0	10.	4	4	6	5	4	3	4	8.8	3	4	6
3	6	2	4	117	0	6	4	3	3	3	7	53	8	6	7
6	8	5	3		6	4	2	9	9	5	1		8	6	4

**Highlights**

- Laboratory  $V_p$  and  $V_s$  measurements conducted up to 600 MPa and 600 °C.
- Contrasting seismic and magnetic anisotropy in amphibolites and gneisses
- Laboratory measurements indicate that intrinsic sources (CPO) govern anisotropy
- Microcracks may contribute up to 20 %, even at middle to low crust conditions.
- Investigation of the relationship between AMS and seismic anisotropy